

Direct ink writing of boron carbide monoliths

Lakhdar, Yazid; Tuck, Christopher; Terry, Anna; Spadaccini, Christopher; Goodridge, Ruth

DOI:

[10.1016/j.jeurceramsoc.2021.08.023](https://doi.org/10.1016/j.jeurceramsoc.2021.08.023)

License:

Creative Commons: Attribution-NonCommercial-NoDerivs (CC BY-NC-ND)

Document Version

Peer reviewed version

Citation for published version (Harvard):

Lakhdar, Y, Tuck, C, Terry, A, Spadaccini, C & Goodridge, R 2021, 'Direct ink writing of boron carbide monoliths', *Journal of the European Ceramic Society*, vol. 41, no. 16, pp. 76-92.
<https://doi.org/10.1016/j.jeurceramsoc.2021.08.023>

[Link to publication on Research at Birmingham portal](#)

General rights

Unless a licence is specified above, all rights (including copyright and moral rights) in this document are retained by the authors and/or the copyright holders. The express permission of the copyright holder must be obtained for any use of this material other than for purposes permitted by law.

- Users may freely distribute the URL that is used to identify this publication.
- Users may download and/or print one copy of the publication from the University of Birmingham research portal for the purpose of private study or non-commercial research.
- User may use extracts from the document in line with the concept of 'fair dealing' under the Copyright, Designs and Patents Act 1988 (?)
- Users may not further distribute the material nor use it for the purposes of commercial gain.

Where a licence is displayed above, please note the terms and conditions of the licence govern your use of this document.

When citing, please reference the published version.

Take down policy

While the University of Birmingham exercises care and attention in making items available there are rare occasions when an item has been uploaded in error or has been deemed to be commercially or otherwise sensitive.

If you believe that this is the case for this document, please contact UBIRA@lists.bham.ac.uk providing details and we will remove access to the work immediately and investigate.

Direct Ink Writing of Boron Carbide Monoliths

Yazid Lakhdar¹, Ruth Goodridge^{1*}, Christopher Tuck¹, Anna Terry², Christopher Spadaccini³

¹ Centre for Additive Manufacturing, University of Nottingham, Nottingham, NG7 2GX, UK

² AWE, Aldermaston, Reading RG7 4PR, UK

³ Lawrence Livermore National Laboratory, 7000 East Avenue, Livermore, CA 94550, USA

* Corresponding author, ruth.goodridge@nottingham.ac.uk

UK Ministry of Defence © Crown Owned Copyright 2021/AWE

LLNL-JRNL-819279

Abstract

Direct ink writing – an extrusion-based additive manufacturing process – followed by pressureless sintering was investigated to produce boron carbide monoliths. The effects of ceramic powder loading and Pluronic binder concentration on the rheology of boron carbide pastes were studied and linked to both processing behaviour and final outcome in terms of sintered density and hardness. The effects of printing parameters, in particular orifice diameter and printing speed, were also investigated. Reducing the size of the extrusion nozzle from 584 μm to 406 μm led to significantly better shape retention, lower surface roughness, as well as higher density and hardness. A 203 μm printing orifice was also trialled but was unsuccessful due to faster drying kinetics that occurred with smaller ceramic struts resulting in rapid warping and nozzle clogging. Carbon-black – 8 wt% relative to B_4C – acted as an effective sintering aid to increase both density and hardness. After optimisation of feedstock and printing parameters, few-layer samples (3-5 layers) had a density as high as $\sim 97\%$ TD and a hardness of ~ 30 GPa. On the other hand, 18-layer specimens had a sintered density of $\sim 87\%$ TD, despite a fully dense microstructure, due to the formation of a 3D array of inter-strut pores. Nevertheless, several issues that arose during manufacturing and post-processing were detrimental to the density and structural integrity of printed specimens; these issues were identified, discussed, and suggestions for future work are provided.

Keywords

Boron carbide

Direct ink writing

Additive manufacturing

Ceramic monoliths

Hardness

1. INTRODUCTION

Boron carbide (B_4C) is an advanced non-oxide ceramic characterised by its extreme hardness, high elastic modulus, low density, high temperature resistance, and excellent neutron absorption. This set of properties make B_4C ideal for a number of engineering applications, including abrasive tools, sand blasting nozzles, radiation shields, and lightweight ballistic armours [1]. Most technical applications of boron carbide require dense sintered monolithic bodies [2] but the densification of B_4C is challenging because of its low plasticity, low self-diffusion coefficient and strong B-C covalent bonding [3]. The manufacture of dense B_4C components for commercial industrial applications is therefore commonly performed by uniaxial hot pressing [4]. However, fabrication techniques based on colloidal processing, such as gel casting, slip casting and additive manufacturing, followed by pressureless sintering, are increasingly gaining in importance as they enable the fabrication of more complex shapes [5][6][7]. Pressureless sintering of B_4C requires the application of small amounts of sintering aids, such as Al [8], ZrO_2 [9], Al_2O_3 [10], and carbon black [11], to enable high apparent densities; an optimised amount of carbon black additive was used in this study.

Direct ink writing (DIW) – also commonly called robocasting [12] – is an AM process in which a highly-loaded viscous ceramic slurry or paste is extruded through a nozzle and solidifies as it is deposited onto a substrate [13]. Suspension solidification and shape retention after deposition are typically induced by the pseudoplastic to dilatant transition that occurs upon evaporation of the solvent [13]. Reversible colloidal gels that coagulate by controlled flocculation with additions of salts or polyelectrolytes and set immediately after deposition without drying can also be used [14][15]. The use of a suitable dispersant, mostly acting by electrosteric repulsion, is essential to the formulation of homogeneous and well-dispersed pastes. Small amounts (0–5 wt%) of other additives, such as thickener, plasticiser and viscosifier, are also added to enhance suspension stability and impart specific rheological properties.

The DIW process relies on the precise control of the rheological properties of the extruded paste. The feedstock must have a high solid loading of well-dispersed ceramic particles in order to minimise shrinkage and to prevent the formation of porosity and cracks during the debinding and sintering heat treatments. They must also have a pseudoplastic (shear-thinning) behaviour to ensure that the very high starting viscosity decreases by several orders of magnitude when subjected to shear inside the extrusion nozzle during deposition [13]. These viscoelastic materials are also designed to have a yield stress and can be fitted to the Herschel-Bulkley model for yield-pseudoplastic fluids [16]. Yield stress increases with the

ceramic solids loading as well as with the addition of binders and stiffening agents such as polyvinylpyrrolidone (PVP) [17], polyethyleneimine (PEI) [18], Pluronic F-127 [19] or methylcellulose [20].

DIW has been used extensively to produce porous biomedical scaffolds for tissue engineering from tricalcium phosphate (TCP) [21][22][23], hydroxyapatite (HA) [24], HA/ β -TCP [25][26][27][28], wollastonite/TCP [29], C-Al₂O₃ [30], bioactive glass [16][31][32][33], and magnesium aluminate (MgAl₂O₄) spinel [34]. DIW has also been used to process a wide range of engineering ceramics, including Al₂O₃ [35][36][37][38][39], PZT [40], mullite [41], barium titanate [18], Si₃N₄ [42][43], SiC [44], and B₄C [45][46][47]. Manufacturing monolithic parts using extrusion-based AM processes present different and additional challenges compared to producing lattice structures. Limited success has been achieved so far in using additive manufacturing to produce dense monolithic parts from carbide ceramics in general, and boron carbide in particular [48]. Nevertheless, DIW is a promising technology to enable the freeform fabrication of dense B₄C with high mechanical properties.

While one of the main advantages of AM processes lies in their ability to produce complex-shaped parts that would be difficult or impossible to fabricate using conventional methods, there remains a need to first demonstrate that AM can be used to produce fully dense and defect-free boron carbide parts using DIW. Indeed, the high mechanical properties of B₄C depend entirely upon the ability to shape defect-free parts of high density (> 95% TD). It is therefore essential to first focus on developing the material and processing routes for the fabrication of fully dense, defect-free B₄C parts, rather than demonstrating complex B₄C components with potentially high defect count and low density, which was already demonstrated in previous studies [45][46]. This study investigated the fabrication of simple boron carbide monoliths using DIW to better understand the relationships between material feedstock composition, rheological properties, DIW parameters, additive manufacturing behaviour, and final properties of green and sintered parts.

First, a range of B₄C pastes using varying ceramic powder loadings and Pluronic binder concentrations were formulated, and their rheological properties – i.e. viscosity, storage modulus, and yield stress – were characterised to identify suitable pastes for DIW operation. It was then essential to optimise printing parameters – namely extrusion orifice diameter, layer height, extrusion pressure and printing speed – according to the specific rheological behaviour of each paste in order to obtain the best possible outcome in terms shape retention, density, roughness and hardness, while minimising printing defects such as drying cracks and internal porosity.

2. EXPERIMENTAL

2.1. Materials

DIW feedstock typically consists of a highly-concentrated aqueous ceramic paste with small amounts of organic additives such as a dispersant and a gelling agent. In this work, B₄C pastes contained the following solid powders: boron carbide powders, carbon black nanopowder and graphene nanoplatelets. B₄C powders were commercially available in grades 1500F and 3000F (3M Technical Ceramics, Germany), which, according to manufacturer's data, had a > 96% purity and an average particle size of approximately 2 μm and 0.5 μm, respectively.

A carbon black powder (Grade C, 150 nm, US-nano.com, USA) was added into the pastes as a sintering aid to assist densification of B₄C during furnace sintering. The amount of carbon black was fixed across all pastes at 8 wt% relative to the mass of boron carbide. A free-carbon concentration of approximately 8 wt% was previously identified by scientists at Lawrence Livermore National Laboratory (LLNL) as a suitable carbon black-to-boron carbide ratio for the given powders [49].

Graphene nanoplatelets (GNPs) with an average surface area of 750 m²/g (xGNP®, grade C-750, XG Sciences Inc., USA) were also added to one of the paste formulations with a view to study their influence on the density, microstructure and mechanical properties of the final components. According to the manufacturer's data, grade C GNP particles typically consist of aggregates of sub-micron platelets with a particle diameter < 2 microns and a typical particle thickness of a few nanometers, with C-750 having a relatively high oxygen content of 8% [50].

First, a branched polyethyleneimine (PEI 25k, MW ~ 25,000, Sigma Aldrich, USA) was added to deionised water, stirred, and left for at least 3 hours to fully dissolve. PEI 25k acted as a cationic dispersant for boron carbide powders in water, and the amount of PEI 25k represented 2.8 wt% relative to the mass of B₄C powder that would be subsequently added, based on previous work by Chandrasekaran et al. at LLNL [47].

B₄C, carbon black and GNP powders were progressively added to water in aliquot parts so as to promote their dispersion in the solvent and prevent excessive formation of particle aggregates and lumps. After each powder batch addition, suspensions were mechanically mixed in a non-vacuum planetary centrifugal mixer (Thinky, USA) at 2000 rpm for 1 min, once at the beginning, and then twice with a 15 seconds cool-off break once pastes were highly concentrated and viscous.

The total mass of resulting pastes was measured, and 1 wt% of stearic acid (ACS reagent, $\geq 99.7\%$, Sigma-Aldrich, USA) was added to adjust the pH of B₄C pastes towards acidic values, since PEI has been shown to be a more effective stabiliser of aqueous B₄C dispersions at pH below 5 [51].

Pluronic powder (Pluronic® F-127, BASF, USA) was added to act as a thickener and stiffening agent. Pluronic F-127, also known as poloxamer 407, is a hydrophilic non-ionic triblock copolymer in an A-B-A configuration where A is a hydrophilic polypropylene glycol (PPG) block and B is a hydrophilic polyethylene glycol (PEG) block. All Pluronic concentrations in this work are expressed as wt% relative to the mass of water in paste formulation.

Four different B₄C formulations were investigated, with varying ratios of B₄C powder grades, carbon black and GNP concentrations, as detailed in **Table 1**. Paste P0, used as the reference, was composed of one B₄C powder grade and was free of carbon additives. An optimised concentration of carbon black was added to paste P1, P2 and P3 to promote sintering densification. Furthermore, a 70/30 wt/wt % ratio of 1500F/3000F B₄C powder grades was chosen to evaluate the impact of a bimodal mixture on packing and sintering density. It was expected that finer particles would fill in the pores formed between coarser particles while also enhancing sintering activity. The ratio was chosen based on results in the literature on ceramic sintering and powder metallurgy where it has been shown that 20 – 50 wt% of the minor powder is usually beneficial to particle packing and densification [52][53].

Table 1: Breakdown of the solids concentration of the four different DIW paste formulations.

Paste formulation	Unit	P0	P1	P2	P3
B₄C 1500F/3000F	wt/wt	100/0	100/0	70/30	70/30
Carbon black	wt% rel. to B ₄ C	0	8	8	8
GNPs	wt% rel. to B ₄ C	0	0	0	1.5

2.2. Methods

2.2.1. DIW setup

The DIW setup was located on a three-axis micropositioning stage (Aerotech, USA). Concentrated aqueous ceramic pastes were loaded into 10 cc syringes equipped with a plunger and a tapered plastic dispensing tip (Optimum® SmoothFlow™, Nordson EFD, USA). A pressure-driven system was used to

deliver the ink through nozzle diameters of either 584, 406 or 203 μm , and the linear feed rate was varied between 2.5 and 10 mm s^{-1} . The extruding pressure in the syringe was varied between 15 and 100 psi (100 and 690 kPa, respectively).

The structures were initially printed on borosilicate glass microscope slides onto which a PTFE release agent dry lubricant was sprayed, or a layer of Vaseline was applied to aid in the release of printed structures from the substrate during the drying process. The structures were allowed to dry out at room temperature for at least 24h before their removal from the substrate. Alternative substrates were then trialled, including a fully dense, smooth ceramic substrate, a fully dense alumina grinding bar with highly rough surfaces, and finally a smooth, 50% porous, green boron carbide disc produced by gelcasting.

2.2.2. Rheological measurements

The rheological properties of DIW pastes were measured on a controlled-stress rheometer (AR 2000ex, TA Instruments, USA) equipped with a cone-and-plate geometry (*cone diameter*: 40 mm; *truncation angle*: 2.006° ; *gap*: 50 μm ; *material*: stainless steel) and a solvent trap to minimise evaporation of water. Pastes were subjected to a continuous oscillation strain sweep test from 0.01 to 100 % strain at a frequency of 1 Hz in order to measure their storage and loss moduli E' and E'' , respectively. The viscosity η was measured by performing a logarithmic shear rate ramp between 1 and 100 s^{-1} at ambient temperature, with twenty measuring points and 50 sec measuring time per decade.

2.2.3. Binder burnout and furnace sintering

Thermogravimetric analysis (TGA 4000, PerkinElmer, USA) was used to determine the content of binder and other organics in B_4C green parts made by DIW. TGA was performed on a sample having a mass of 9.919 grams, under a constant nitrogen gas flow of 19.8 ml/min, from 30°C to 600°C with a heating rate of $20^\circ\text{C}/\text{min}$. Furnace sintering is a crucial step when attempting to manufacture high density advanced ceramic parts. TGA of a DIW green sample, provided in Supporting Information, revealed that organics (PEI and Pluronic) were completely removed from green parts at 500°C (SI-1); this temperature was thus chosen for the debinding step.

Binder burnout was carried out by carbonising green parts in an oven (Carbolite Gero Ltd, UK) at 500°C in argon atmosphere using heating and cooling rates of 20°C per hour. Samples were then sintered in a high-temperature vacuum furnace (Carbolite Gero Ltd, UK) under argon gas using a $300^\circ\text{C}/\text{h}$ heating rate up to 2275°C with a 1 h hold at T_{max} , followed by a natural cool down to T_{ambient} .

2.2.4. Post-printing characterisation and testing

2.2.4.1. Dimensions, mass, and density of 3D printed specimens

Geometric measurements of green and sintered 3D printed samples were made using a digital calliper (± 0.002 mm). Dimensions of each sample in X, Y, and Z were averaged out of three locations in each direction. The mass of each sample was measured on a Mettler Toledo XS104 analytical balance. The density of the sintered ceramic specimens was measured by water immersion according to Archimedes' principle described in ASTM Standard B311-13 [54]. The theoretical density was calculated according to the rule of mixtures taking into account the amount of different sintering additives present in each sample.

2.2.4.2. Micro computed tomography (μ CT) scanning

X-ray micro computed tomography (μ CT) scanning was conducted on a Bruker SkyScan 1172 instrument. Three samples with approximate dimensions $10 \times 10 \times 5$ mm³ were imaged using a medium camera (2000 pixels) and the following parameters: 54 – 60 kV voltage, 7 W power, 8 frame averaging, and 10 random movements with 11.89 μ m resolution. Subsequent analysis was conducted using the associated software (NRecon, Dataviewer, CTAn, CTVox). Images were produced based on the pre-set colour scheme labelled 'ammonite'.

2.2.4.3. X-ray diffraction (XRD)

XRD analysis was performed in order to assess which phases were present in as-printed green samples and in final sintered specimens. XRD was performed on a D8 Advance diffractometer (Bruker Corporation, USA) equipped with the DIFFRAC.SUITE EVA software for data treatment and analysis. Measurements consisted of 5 min-long scans carried out on rotating samples using a Bragg-Brentano / Divergent Beam with $10 - 80$ in 2θ range, 0.02° step size, and 0.1 s at each data point.

2.2.4.4. Surface roughness

The surface roughness of two $10 \times 10 \times 4$ mm³ sintered rectangular cuboids that were printed with the 584 and 406 μ m diameter nozzles, respectively, was measured using a stylus surface profilometer (Form Talysurf Intra, Ametek Taylor Hobson Ltd, USA) equipped with a surface analysis software (MountainsMap, Digital Surf, France). Measurements were taken on the top, bottom and lateral surfaces of samples along a 5 mm-long straight line on each surface. The surface form was extracted from the original profile using a Gaussian filter with a 0.8 cut-off.

2.2.4.5. Vickers hardness

The top surface of the sintered B₄C specimens was subjected to grinding using successively finer grinding discs (from 400 grit to 1200 grit) followed by polishing using a diamond paste. The hardness of sintered specimens was measured by way of a Vickers hardness indentation technique on a Wilson® VH3100 (Buehler, USA) equipped with a pyramidal diamond tip. Indentation tests were performed on ground and polished sample surfaces under a load of 1 kgf (9.8 N) with a dwell time of 10 s, as per ASTM standard C132715 [55].

3. RESULTS

3.1. Paste formulation, rheological behaviour and printing outcome

3.1.1. Ceramic powder loading

Several slurry formulations were prepared with increasing ceramic powder loading from 46 to 49 vol%, while keeping a constant Pluronic concentration of 10 wt% relative to the mass of water in slurry. As expected, the viscosity of slurries increased with increasing solids loading, and all formulations exhibited a pseudoplastic behaviour (**Figure 1**). It can also be noticed on the storage modulus curves that the slow two-step decrease of E' displayed by the 46 vol% paste was progressively mitigated as the solids loading was increased up to 49 vol% B₄C, which displayed a much sharper drop of E' and therefore a faster transition from elastic to viscous behaviour. Furthermore, it can also be noted that both the storage modulus and the yield point (the value of the shear stress at the limit of the linear viscoelastic region) increased with increasing solids loading.

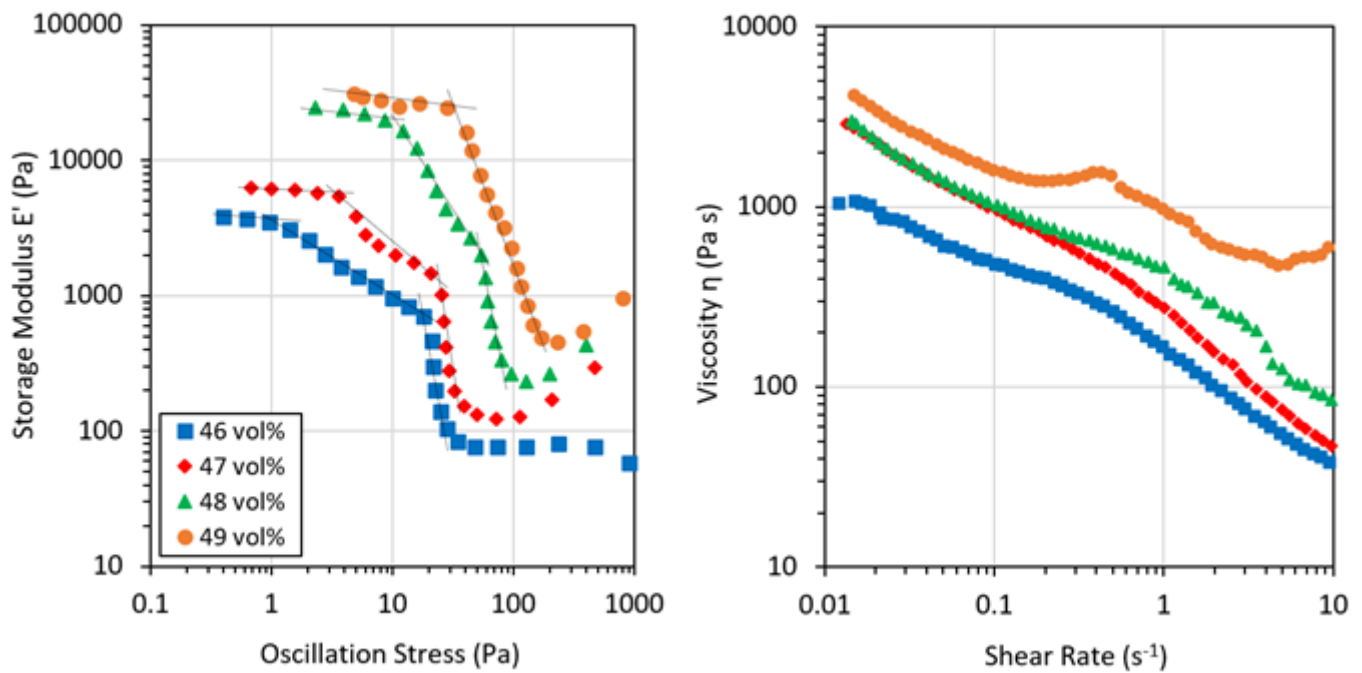


Figure 1: Rheological properties of B₄C pastes of various ceramic powder loadings, showing an increase in viscosity, storage modulus and yield stress as the solids loading is increased.

B₄C pastes could be divided into two groups with regards to the direct influence of rheological properties on DIW behaviour. On the one hand, the 46 and 47 vol% B₄C slurries with 10 wt% Pluronic could not be processed at all using DIW because of their rheological behaviour. Indeed, although these slurries could be extruded initially, they would keep on dripping out of the extruding orifice even as the printing process was paused. This was caused by their low yield stress as well as by their apparent two-step decrease in storage modulus (**Figure 1**) pointing to a lack of a clear yield stress value separating the elastic and viscous domains. Second, struts deposited onto the substrate were not able to hold the intended shape due to low stiffness (E' value) and low viscosity. On the other hand, the 48 and 49 vol% pastes could be extruded in a controlled fashion due to their higher yield stress and storage modulus, although extruded struts were not stiff enough nor did they harden quickly enough to enable the layerwise production of monolithic 3D structures. Moreover, nozzle clogging was experienced with all of these slurries as soon as the DIW process was paused or stopped for any reason. It was then not possible to carry out any further printing due to drying inside the extruding tip, thus preventing material extrusion even as the pressure inside the syringe was brought up to the maximum syringe pressure of the DIW apparatus.

3.1.2. Pluronic concentration

Following the study of the effect of solids loading on the rheology and DIW behaviour of B₄C pastes, the influence of binder concentration was then investigated. Several slurries of identical starting composition were prepared – 45 vol% B₄C powder grade F1500 with 8 wt%/B₄C of carbon black additive and 2.8 wt%/B₄C of PEI dispersant – and the concentration of Pluronic was varied. The oscillatory stress amplitude sweep response of these slurries is presented in **Figure 2**. First, while pastes containing both 15 and 17 wt% Pluronic had a similar starting value of storage modulus as the slurry containing only 10 wt% Pluronic (~ 1,500 – 2,000 Pa), further increasing the Pluronic addition to 18 wt% resulted in a significantly stiffer paste with a higher storage modulus (~ 4,750 Pa). Moreover, the 10 wt% Pluronic slurry exhibited a two-step decrease of E' that occurred over a wide range of applied stresses, while slurries containing 15–18 wt% Pluronic exhibited a sharp drop of the storage modulus. This sharp and well-defined drop of E' represents the ideal behaviour for selective extrusion as it means the structural integrity of the paste is lost and recovered almost immediately as the paste is subjected to a stress above and below the yield stress, respectively. Furthermore, similarly to the effect of increasing solids loading, higher Pluronic concentration also resulted in higher yield stress.

Another common way to define the stress at which a paste starts to flow is called the flow point, which is defined as the crossover point where the loss modulus (E'') overcomes the storage modulus (E'). The loss modulus is also provided in **Figure 2** for reference.

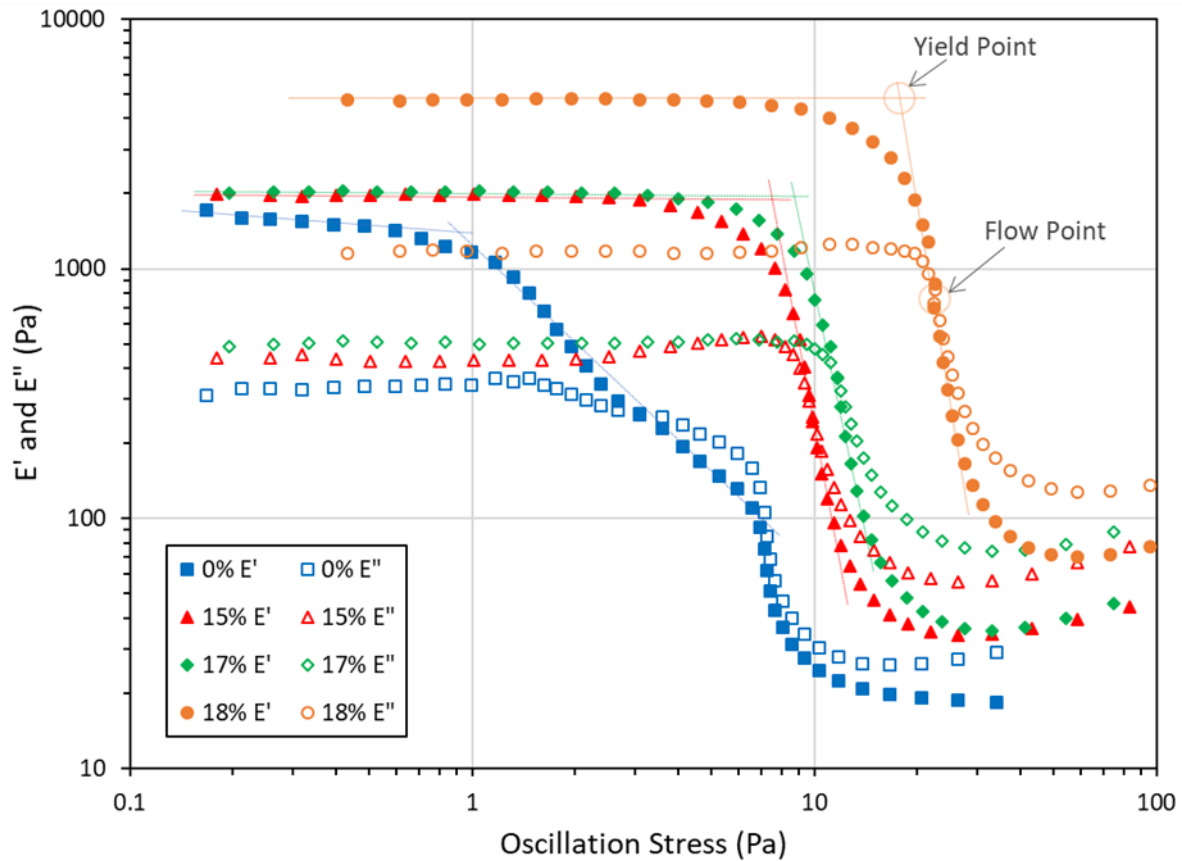


Figure 2: Oscillatory strain sweep response of 45 vol% B₄C slurries containing various wt% of Pluronic.

While previous slurries that contained 10 wt% Pluronic dried out prematurely at the nozzle tip, thus causing clogging, this issue was not experienced once the Pluronic concentration was increased to 15 wt%. Therefore, Pluronic not only acted as a viscosifier and stiffening agent, but it also performed the function of humectant. However, these slurries still experienced the same printing issues, namely extruding out of the nozzle uncontrollably even as the syringe pressure was turned off, as well as a lack of structural stiffness of deposited struts, due to their low storage modulus $E' < 10,000$ Pa. Indeed, while the increase in Pluronic concentration to 18 wt% caused a significant increase in both stiffness and yield stress, these values remained relatively low, at approximately 4,700 Pa and 16 Pa, respectively, due to the low solids loading of the starting slurry (45 vol%).

Thus, although overlapping struts could be deposited to produce small 3D monolithic structures, ceramic layers deposited using these formulations were subjected to significant deformation during printing and had very slow drying kinetics due to their large water content and low binder concentration. In particular, because of the low stiffness of deposited struts, the layer being printed (L) would not have

enough support from the previous layer (L-1), resulting in merging of the layers and deformation of the structure as the extruding tip dragged previous layers with it (**Figure 3.a**).

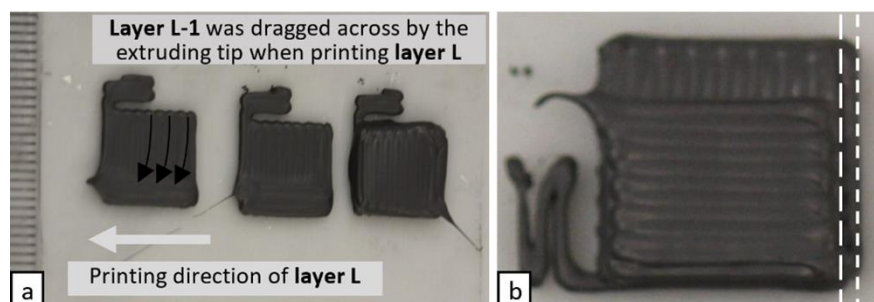


Figure 3: Two-layer monoliths produced by DIW of a 45 vol% B₄C slurry with 18 wt% Pluronic through a 584 μm orifice experienced deformation and slumping due to the low viscosity of the paste (a). Paste deposition was shifted compared to its intended location due to a lack of bonding with the previous layer when depositing a stiff [48 vol% B₄C / 17 wt% Pluronic] paste at high travel speeds (b).

3.1.3. Optimising paste formulation for successful DIW operation

In order to yield more viscous pastes with a higher storage modulus and a higher yield stress, while containing enough binder to prevent premature slurry drying and nozzle clogging, a combination of increased solids loading > 46 vol% with a Pluronic concentration of at least 15 wt% was required.

In order to narrow down the number of paste formulations suitable for DIW operation, various pastes with solids loading ranging from 46 vol% to 50 vol% and with a Pluronic concentration between 15 wt% and 21 wt% were prepared; their printing behaviour was assessed and the rheological properties of pastes that could be processed successfully by DIW were then characterised.

First, all the pastes that contained more than 17 wt% Pluronic relative to liquids were too viscous and too stiff to be extruded, independently of their solids loading. The suitable range of Pluronic concentration was thus narrowed down to 15 – 17 wt%. Second, all the 50 vol% pastes were also too viscous to be extruded independently of their Pluronic concentration. The suitable range of solids loading was thus narrowed down to 47 – 49 vol%. All other formulations containing a ceramic powder content of 47 – 49 vol% and a Pluronic concentration of 15 – 17 wt% could be extruded on-demand without suffering from nozzle clogging and were therefore used to produce 3D monoliths. Identical Pluronic concentration levels were found to have the same effect on paste viscosity and extrudability irrespective of powder mix.

Figure 4 shows that the rheological properties of 47 vol% and 48 vol% B₄C pastes were significantly modified by increasing their Pluronic concentration from 10 wt% to 15 -17 wt%, resulting in higher values

of viscosity, storage modulus and yield stress. Although both the [47 vol% B₄C / 15 wt% Pluronic] and the [48 vol% B₄C / 17 wt% Pluronic] pastes could be processed by DIW to manufacture small monoliths, their printing behaviour was far from identical. Thus, printing parameters had to be continuously adjusted and optimised for each feedstock formulation in order to account for their respective rheological properties. A high stiffness was desirable for struts to solidify and retain their shape upon deposition in order to avoid structural slumping and provide a solid support for subsequent layers. However, pastes of high stiffness required lower deposition speeds to form a continuous strut and to achieve inter-layer bonding, especially in locations where the extrusion orifice would change direction. Indeed, a printing defect in the form of a void or disconnected strut commonly occurred when depositing stiff pastes at high travel speeds, as evidenced in **Figure 3.b**, where the paste was dragged by the nozzle when it changed direction to print a new line. This defect was easily addressed by decreasing the travel speed of the nozzle to allow for the paste to bond to the previous layer before initiating a change of direction.

The [47 vol% B₄C / 15 wt% Pluronic] and [49 vol% B₄C / 10 wt% Pluronic] pastes had a very similar storage modulus curve, although the former paste had a higher viscosity at low shear rates.

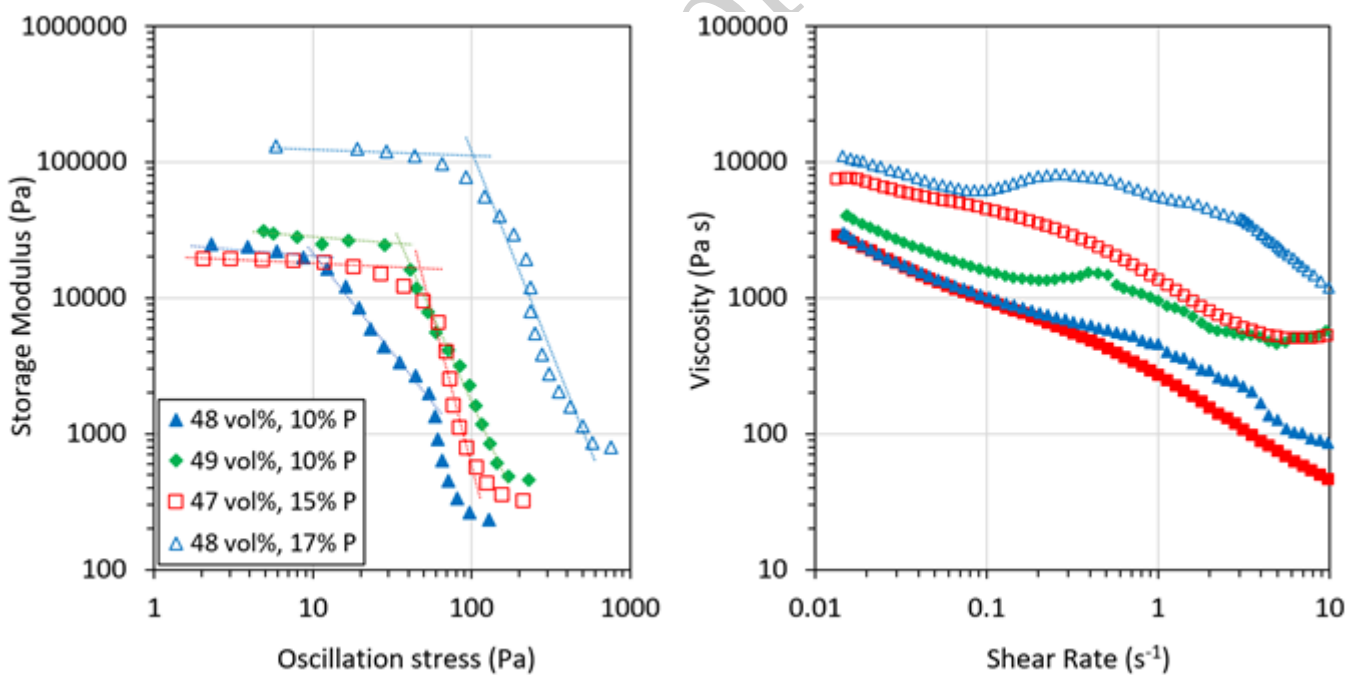


Figure 4: Storage modulus and viscosity plots showing the combined effects of varying ceramic powder loading and Pluronic concentration on the rheological properties of aqueous B₄C pastes.

The rheological behaviour of four different pastes formulated from a starting paste of given ceramic loading (49:51 B₄C/water v/v) with increasing Pluronic binder concentration is reported in **Figure 5**. These four pastes were selected to broadly represent the four possible scenarios that occurred during DIW operation.

The first paste (**F1**) represented the typical starting paste formulation before addition of the Pluronic binder. These ceramic pastes, not yet optimised for extrusion, were characterised by a much lower viscosity ($\sim 15 \text{ Pa s}$ at 10 s^{-1}), a significantly lower storage modulus ($< 10,000 \text{ Pa}$), and a considerably lower yield stress ($\sim 3 \text{ Pa}$) than pastes containing Pluronic. This type of paste was too fluid at both low and high shear rates to be selectively extruded, and led to complete clogging of the extruding orifice.

The second paste (**F2**) had Pluronic added to a concentration of 12 wt% relative to the mass of water, which was below the ideal Pluronic concentration range defined previously (15–17 wt%). At this concentration, however, the paste had a higher storage modulus ($\sim 28,000 \text{ Pa}$) and higher yield stress ($\sim 43 \text{ Pa}$) that enabled selective extrusion at low syringe pressures of 15 – 20 psi (100 – 140 kPa) and high travel speed ($> 5 \text{ mm/s}$). These pastes experienced high merging of individual struts but also significant slumping upon deposition due to slow drying kinetics. These characteristics made them unsuited to build small structures. Indeed, as there was a short time between successive passes of the nozzle at any given point, there was not enough time for previous layers to stiffen and provide a solid support. On the other hand, this paste was relatively suited to producing higher aspect ratio structures such as beams, since enough time would elapse between successive nozzle passes for the deposited paste to dry out and stiffen. However, this paste resulted in significant drying cracks during deposition and was prone to drying at the nozzle tip due to its low Pluronic concentration, resulting in nozzle clogging.

The third paste formulation (**F3**) had a higher Pluronic concentration of 15 wt% relative to the mass of water, which resulted in an increase of the storage modulus by 100% to $\sim 58,000 \text{ Pa}$ and of the yield stress by 50% to 64 Pa. This paste could be successfully deposited selectively using higher syringe pressures of 50 – 60 psi (350 – 420 kPa) and at lower travel speeds (4 – 5 mm/s) than the previous paste.

Finally, the last paste (**F4**) represented the rheological behaviour of high solids loading pastes with excessive Pluronic concentration (21 wt%) that resulted in a high stiffness $> 100,000 \text{ Pa}$, which in and of itself could be considered ideal for shape retention upon deposition. However, with a yield stress of almost 600 Pa, this paste could not be extruded. An ideal paste for DIW operation would therefore have characteristics somewhat in between that of the last two pastes, with a yield stress of $\sim 100 \text{ Pa}$ similar to that of **F3** and a storage modulus above 100,000 Pa similar to that of **F4**; these properties correspond to the paste formulation [48 vol% B₄C / 17 wt% Pluronic].

An overview of the main characteristics of the B₄C paste formulations of various solids loading and Pluronic concentration that were investigated for DIW is presented in **Table 3**.

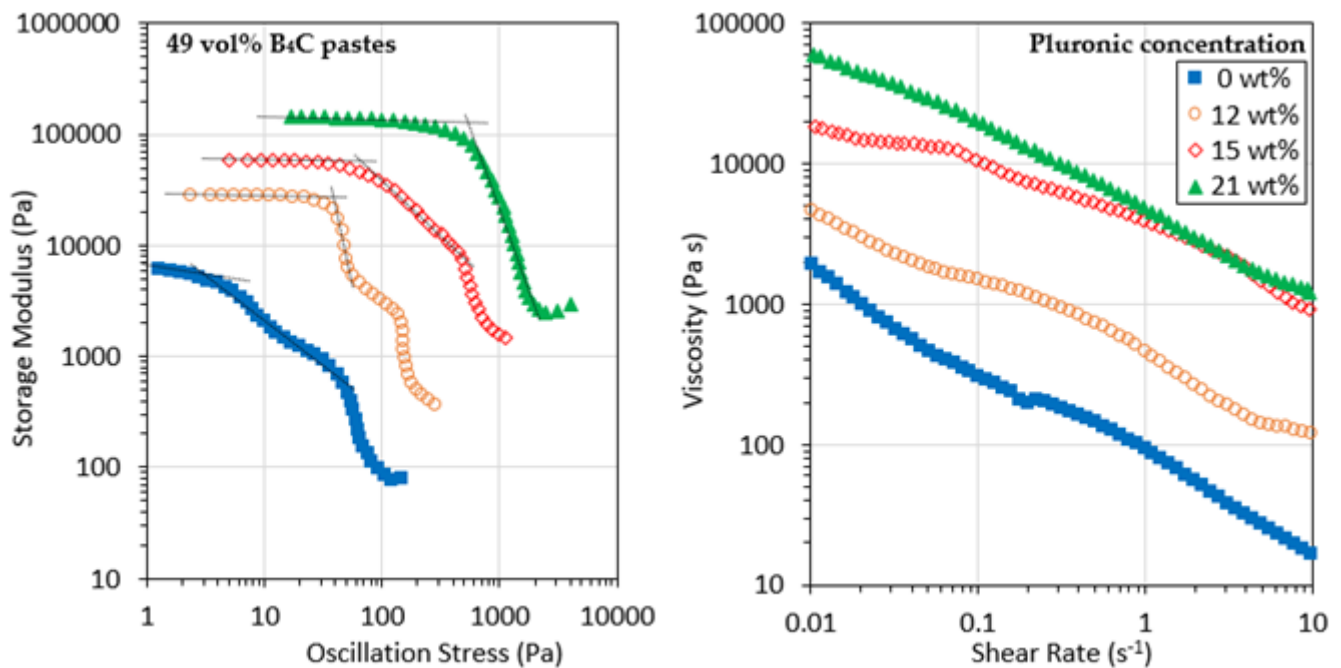


Figure 5: Rheological behaviour of 49 vol% B₄C pastes with various Pluronic concentrations: 0 wt% (F1), 12 wt% (F2), 15 wt% (F3), and 21 wt% (F4).

Table 2: Combined impact of solids loading and Pluronic concentration on the main rheological characteristics of B₄C pastes for DIW. Pastes that could be successfully extruded and shaped are highlighted in bold.

Solids loading [vol%]	Pluronic conc. [wt%]	Elastic plateau [kPa]	Yield stress [Pa]	Viscosity at 0.1 s ⁻¹ [kPa s]
46	10	3.7	1	0.47
47	10	6	4	1
47	15	19	40	4.4
48	10	23	10	1.06
48	17	120	100	6.3
49	0	6	3	0.29
49	10	25	37	1.5
49	12	28	50	1.45
49	15	58	64	10
49	21	140	570	20

3.2. DIW printing parameters and printing outcome

3.2.1. Extrusion pressure

The extrusion pressure was the first parameter that needed to be modified and adjusted when attempting to process a new paste by DIW. First, the minimum pressure P_{\min} that enabled to overcome the yield stress of ceramic pastes and induce flow out of the extrusion orifice had to be identified. P_{\min} increased with increasing solids loading and binder concentration as both variables resulted in higher yield stress (**Figure 4**). The suitable range of extrusion pressure for a given paste was therefore any pressure P so that $P_{\min} \leq P \leq P_{\max}$, where P_{\max} was the maximum pressure that could be exerted onto the syringe barrel. Then, as the pressure was varied within that range, the printing speed had to be optimised accordingly so that a good match between pressure and speed was obtained in order to consistently produce struts of appropriate width and height for 3D shaping.

3.2.2. Optimising deposition speed

Deposition speed – namely the linear travel speed of the extrusion nozzle in the X-Y plane and in the Z direction – had a significant influence on the printing outcome. The optimisation of deposition speed went hand-in-hand with that of pressure in order to avoid both “under-pumping”, namely the situation where a strut of reduced diameter $d_{\text{strut}} < d_{\text{orifice}}$ is produced due to the deposition speed being too fast for the rate of extrusion of the paste. “Over-pumping” is the opposite situation where $d_{\text{strut}} > d_{\text{orifice}}$ because the travel speed is too low for the extrusion pressure. Therefore, for a paste of given minimum extrusion pressure P_{\min} corresponded an ideal printing speed S_{\min} ; the printing speed had to be increased as the pressure was increased towards P_{\max} , in order to prevent both under- and over-pumping.

Figure 6 shows an example of how a small modification of printing speed, while keeping other variables constant, would result in a vastly different outcome. Specimens printed using the 584 μm nozzle lost in structural integrity as the speed was increased from 5.75 mm/s to 7.5 mm/s, with the formation of gaps between deposited lines due to under-pumping (B1) and with poor shape retention and significant slumping at the edges (B2).

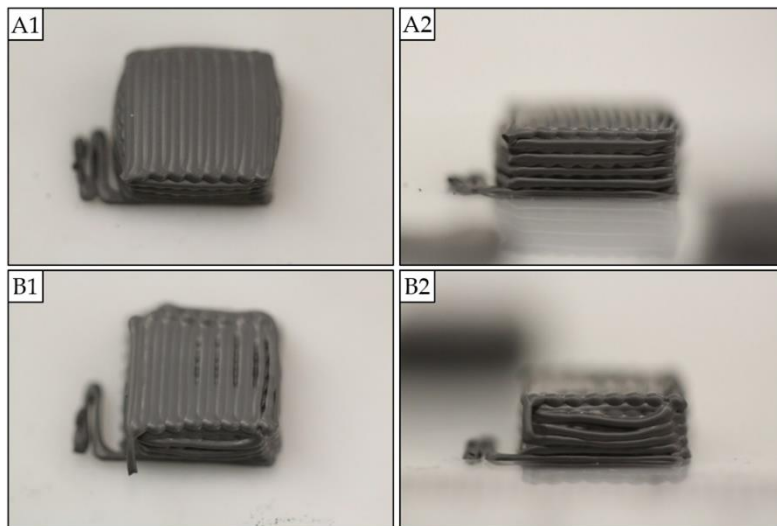






Figure 6: 10-layer 10×10 mm² monoliths produced by DIW using a 584 μm orifice diameter, 440 μm layer thickness, 40 psi (280 kPa) syringe pressure, and a deposition speed of 5.75 mm/s (**A1, A2**) or 7.5 mm/s (**B1, B2**).

The typical process for optimising travel speed so as to obtain the best possible printing outcome is detailed in **Table 3**. A 10-layer monolithic shape was produced from a paste of given formulation using set values of orifice diameter, layer height and syringe pressure, while iteratively adjusting the transverse speed of the printing nozzle according to visual observation and qualitative assessment of the printing outcome. This iterative process enabled identification of the printing speed that gave the best match between printing speed and extrusion pressure and would produce a pore-free structure with dimensions as close as possible to the digital model without creating printing defects.

Table 3: Optimisation process of printing speed to obtain the best possible outcome with all other printing variables kept constant (intended geometry was $10 \times 10 \times 4 \text{ mm}^3$).

Fixed parameters	Orifice diameter: 584 μm			
	Layer height: 440 μm			
	Syringe pressure: 80 psi (550 kPa)			
Printing speed	2.5 mm/s	4 mm/s	5 mm/s	6 mm/s
Top view of printed structure				
Match between printing speed and extrusion pressure	Significant over-pumping	Slight over-pumping	Best match	Slight under-pumping
Porosity	No visible porosity	No visible porosity	No visible porosity	Inter-strut porosity
Green dimensions (mm^3)	$11.6 \times 11.5 \times 3.3$	$10.7 \times 10.3 \times 4.1$	$10.5 \times 10.3 \times 4.0$	$10.2 \times 10.2 \times 4.1$
Additional observations on shape retention	Spreading and flattening effect caused by high pressure.	Significant slumping. Bulging of top surface.	Slight slumping. No bulging of top surface.	Good retention of shape and dimensional accuracy.

3.2.3. Printing orifice diameter

The diameter of the printing orifice had a significant influence on the selection of suitable printing parameters, as well as on the appearance of printed parts, in particular shape retention, resolution and surface roughness. The following nozzle diameters were investigated: 584, 406, and 203 μm .

Geometrical accuracy, shape retention and resolution were greatly affected by the diameter of the extrusion orifice. When printing with the larger nozzle (584 μm), internal forces were caused by slumping and increasing sample deformation with layer count, because struts did not dry fast enough due to the high volume-to-surface ratio, resulting in the surface of struts drying out while a large volume of paste remained wet at the core. This issue was largely improved by using a finer extruding tip (406 μm), which enabled the production of finer struts of not only lower weight but also reduced volume-to-surface ratio, leading to stiffer lightweight struts that dried out quicker, ultimately resulting in less structural slumping.

Figure 7 shows the best outcome that was achieved when printing with the 584 and 406 μm tip diameters, respectively. In particular, much less material slumping and sharper vertical edges were observed with the 406 μm orifice, which combined with the higher resolution provided by the finer extrusion nozzle resulted in much flatter top and side surfaces and overall better shape retention.

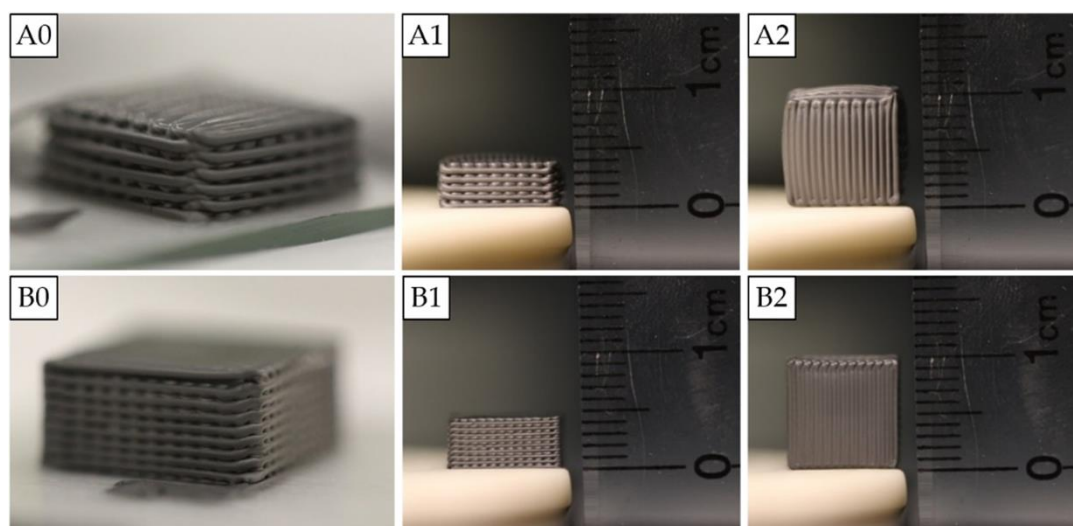


Figure 7: B₄C green parts produced using the 584 μm (A0) and 406 μm (B0) extrusion orifices; better resolution and shape retention were achieved with the finer extrusion nozzle. Side view (A1, B1) and top view (A2, B2). Printing parameters: 47 vol% B₄C paste, 80 psi (550 kPa) syringe pressure, 4 mm/s deposition speed, and 440 μm layer height (A); and 47 vol%, 30 psi (200 kPa), 4 mm/s, and 260 μm , respectively (B).

3.3. Macro- and micro-porosity

Despite their fully-dense appearance (**Figure 7**), most monolithic samples were characterised by the formation of macro- and/or micro-pores that originated from the bottom surface, as shown in **Figure 8**. This porosity was caused by trapped solvent due to slow solvent drying kinetics that resulted in material displacement as layers were deposited one on top of the other. This was found to be influenced by feedstock composition, size of the extrusion orifice, and substrate morphology.

3.3.1. Feedstock composition and size of the extrusion orifice

The smaller nozzle was found to result in much lower porosity and reduced pore size at the bottom surface, as evidenced in **Figure 8**, showing parts produced using the 584 μm nozzle (A and B) compared to parts made with the 406 μm nozzle (C and D).

Paste formulation also had a significant effect on the extent of porosity formed at the bottom surface of printed components. Indeed, significantly bigger pores were formed when shaping a paste with 46 vol% B_4C (A and C) compared to a 48 vol% formulation (B and D). Furthermore, the size of drying cracks was also significantly reduced when using the higher loading paste in the case of printing with the 584 μm nozzle (A compared to B), while drying cracks were completely eliminated when using the smaller nozzle (C compared to D).

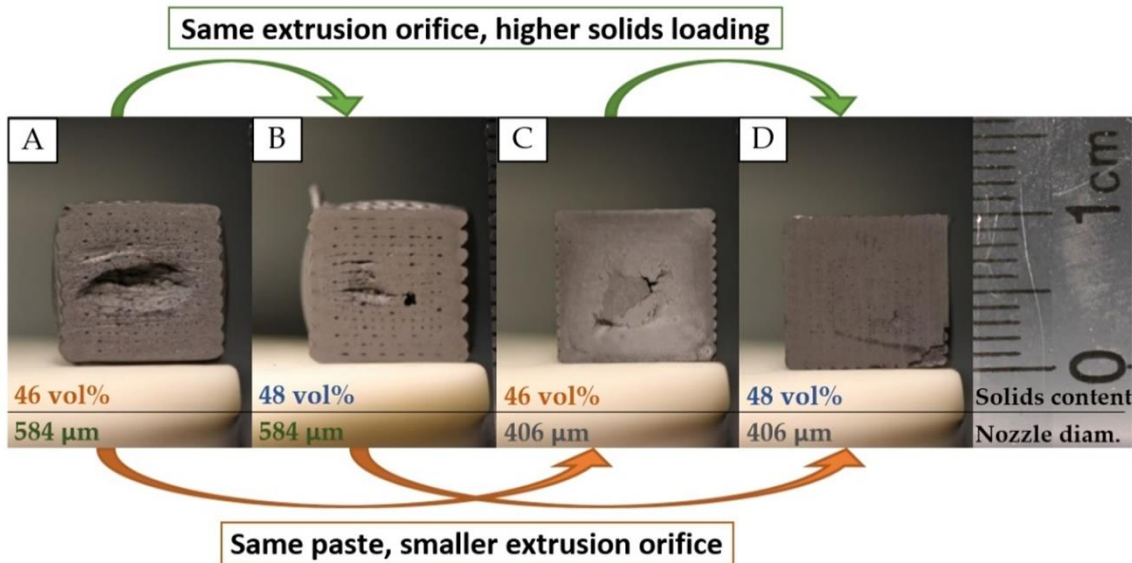


Figure 8: Bottom surface of multi-layer B_4C monoliths manufactured by DIW using an extruding tip diameter of 584 μm (A, B) and 406 μm (C, D), when shaping a 46 vol% (A, C) or a 48 vol% (B, D) paste (of identical Pluronic concentration).

CT scanning provided valuable information on the internal structure of multi-layer printed samples, in particular with regards to the level of internal porosity. Indeed, while some samples seemed to exhibit a near fully dense and defect-free structure upon external inspection, very large voids and significant cracking could in fact be observed internally, as evidenced in **Figure 9**. This issue occurred in most specimens due to the lack of evaporation pathways for the solvent at the centre of printed structures leading to mass transports from the centre as water travelled through samples towards the surface as it dried. Nonetheless, this issue could be significantly minimised by optimising the materials and printing parameters. One way this could be fully avoided would be by stopping the print after each layer to give enough time for each layer to dry out and solidify before depositing the subsequent layer; however, this solution is obviously not viable as it would result in considerably longer printing times.

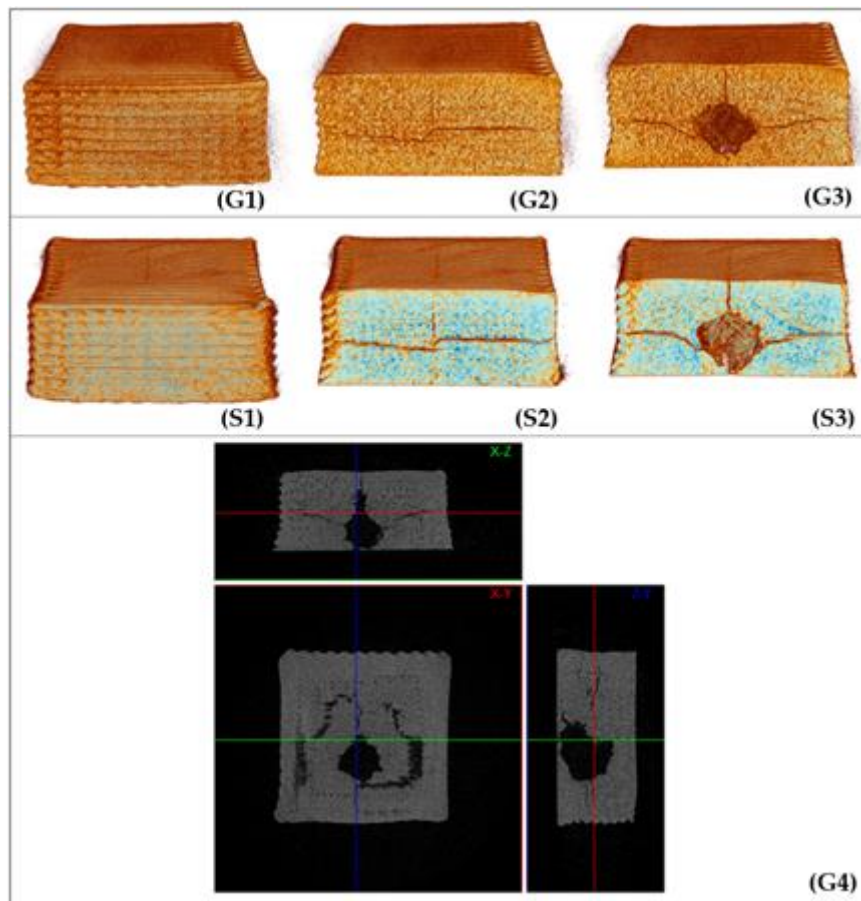


Figure 9: μ CT scan of a $10 \times 10 \times 4 \text{ mm}^3$ monolithic B_4C sample in the green (G) and sintered (S) states produced from a 46 vol% paste using a $406 \text{ }\mu\text{m}$ diameter nozzle, showing how an apparent monolith from external observation (G1, S1) may have developed extensive internal macro-cracking (G2, S2) caused by large internal porosity (G3, S3, G4).

3.3.2. Printing substrates

Another route that was investigated to improve the density of monoliths involved depositing ceramic pastes onto various substrates that could physically interact with the solvent and affect its evaporation rate in various ways. Thus, four different printing substrates were investigated in an attempt to mitigate the critical porosity observed in **Figure 8**. **Figure 10:** DIW of B_4C pastes was carried out onto a variety of substrates: fully-dense, smooth glass slide (A), dense, smooth silicate ceramic (B), fully dense, rough alumina bar (C), and 50% porous, smooth boron carbide puck (D). A picture of the printing process onto each substrate is provided in **Figure 10**, along with the main physical characteristics of these four substrates. All the substrates were sprayed with a thin layer of PTFE coating before DIW operation.

DIW prints were initially all produced onto smooth borosilicate glass slides (**Figure 10.A**). Printing onto a near dense silicate ceramic plate (**Figure 10.B**) resulted in the same outcome as the glass slide, namely

dense monoliths in appearance (**Figure 11.A**) that were affected by the formation of macro porosity originating at the centre of the bottom surface due to the lack of evaporation pathway for the solvent. However, printed parts were more easily removed from this substrate than from glass slides.

A rough alumina grinding bar (**Figure 10.C**) resulted in the same printing defects. However, the high surface roughness of alumina bars caused two additional issues. First, it was more difficult to remove printed parts from this substrate because the high surface roughness provided more physical anchoring points for bonding. Secondly, since the roughness of the bottom surface of printed parts is a function of the surface roughness of the substrate, these specimens were significantly more rough than that of parts deposited onto the previous two smooth surfaces.

A 50% porous green B₄C puck made by gelcasting (**Figure 10.D**) was also used as printing substrate, which led to completely different drying behaviour and printing outcome compared to previous substrates. The drying rate – recorded by visual observation – of 10×10 mm² square single layers printed onto this 50% porous substrate was compared to that of identical layers deposited onto dense substrates. On average, layers dried out completely in 6'57" ± 23" on glass slides, while it took 6'11" ± 18" on the dense silicate ceramic substrate. On the other hand, it took only 4'08" ± 09" for layers to dry on the porous B₄C substrate. The solvent was likely wicked out of the sample through pores in the substrate when using the 50% porous substrate, which accelerated drying. However, this highly accelerated drying rate on the porous B₄C substrate – on average 40% faster than onto glass slides – also resulted in an aggressive and almost immediate warping up of deposited ceramic layers as they were drying, as evidenced in **Figure 11.B**, making this substrate unsuitable for part manufacturing. The dense silicate ceramic substrate also resulted in a slightly accelerated drying rate compared to glass slides – 11% faster on average – without causing any warping of parts; however, the formation of pores at the bottom surface of printed parts still occurred.

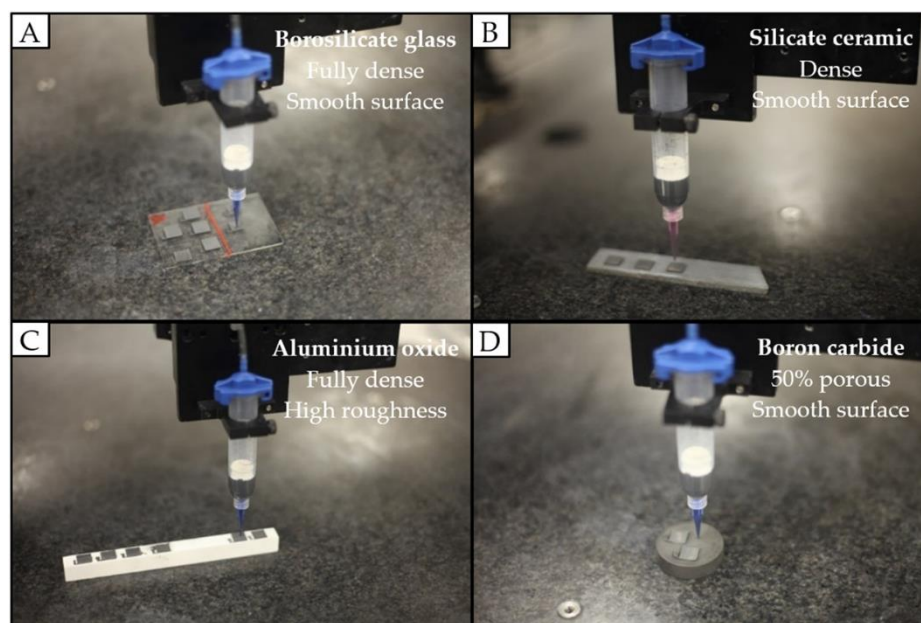


Figure 10: DIW of B_4C pastes was carried out onto a variety of substrates: fully-dense, smooth glass slide (A), dense, smooth silicate ceramic (B), fully dense, rough alumina bar (C), and 50% porous, smooth boron carbide puck (D).

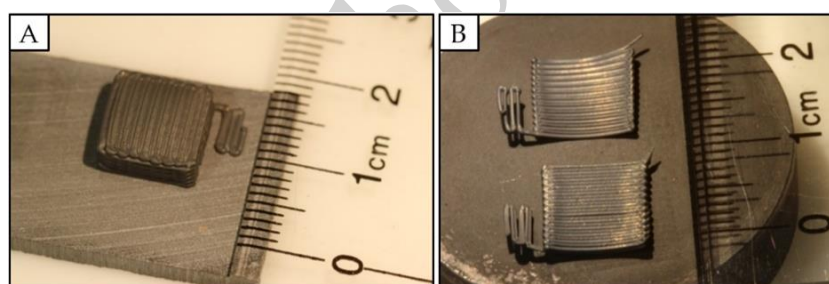


Figure 11: Close-up of a $10 \times 10 \times 4 \text{ mm}^3$ B_4C monolith printed onto a dense silicate ceramic substrate (A). B_4C layers deposited onto a 50% porous B_4C puck experienced aggressive warping upon drying out due to solvent wicking into the pores in the substrate (B).

3.4. Sintering, density and microstructure

Figure 12.A displays, side by side, a green and a sintered part manufactured from the same 3D model, showing the reduction in size and change of appearance of B_4C parts after firing. On average, monolithic sintered specimens shrank laterally and vertically by $\sim 16 \pm 1 \%$, $15 \pm 1 \%$, and $\sim 20 \pm 1 \%$ in the X, Y, and Z direction, respectively. The average volumetric sintering shrinkage was 43 %.

A photograph of the bottom surface of the sintered sample is also shown in **Figure 12.B**, highlighting the apparent high density of the part although 4 macro-cracks were clearly visible near the centre of the

surface. These cracks were formed during the pressureless sintering step and originated from internal porosity located just above the bottom layer formed during drying after deposition due to solvent removal issues. Printing lines were also clearly visible on the surface.

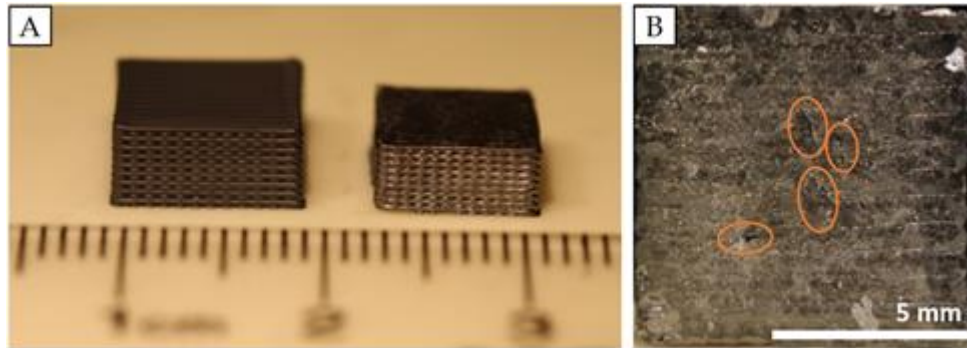


Figure 12: B_4C samples in the green state (left) and after pressureless sintering (right) (A). Printing lines were visible on the bottom surface of sintered samples and cracks, highlighted by the orange ovals, could be observed near the centre of the surface (B).

As shown in **Figure 13**, **Figure 13: SEM images of the** internal structure of a sintered B_4C beam fabricated from a paste formulation without C sintering aid, showing regularly spaced macro-pores between struts and a very high level of residual micro-porosity. internal macro-porosity also occurred in the form of a three-dimensional array of inter-strut pores, about 200 μm wide, likely caused by excessive contraction of deposited filaments upon drying and by poor inter-strut bonding.

Figure 14.a-b show photographs of a DIW monolithic beam before and after furnace sintering, respectively; the beam was fabricated using the optimised paste formulation [47 vol% B_4C , 17 wt% Pluronic] with 8 wt% carbon black relative to B_4C . The same 3D array of macro-pores occurred in these beams, as shown in **Figure 14.c**, although pores were significantly smaller ($\sim 100 \mu\text{m}$). Nevertheless, carbon sintering aids greatly improved the density of B_4C specimens, as observed when comparing the SEM images of fracture surfaces: the former was characterised by a very high level of residual microporosity (**Figure 13**) whereas the latter had a near-fully dense microstructure (**Figure 14.d-g**). This demonstrated again that optimising paste formulation was extremely important not only to enable the printing process itself but also to obtain dense monoliths.

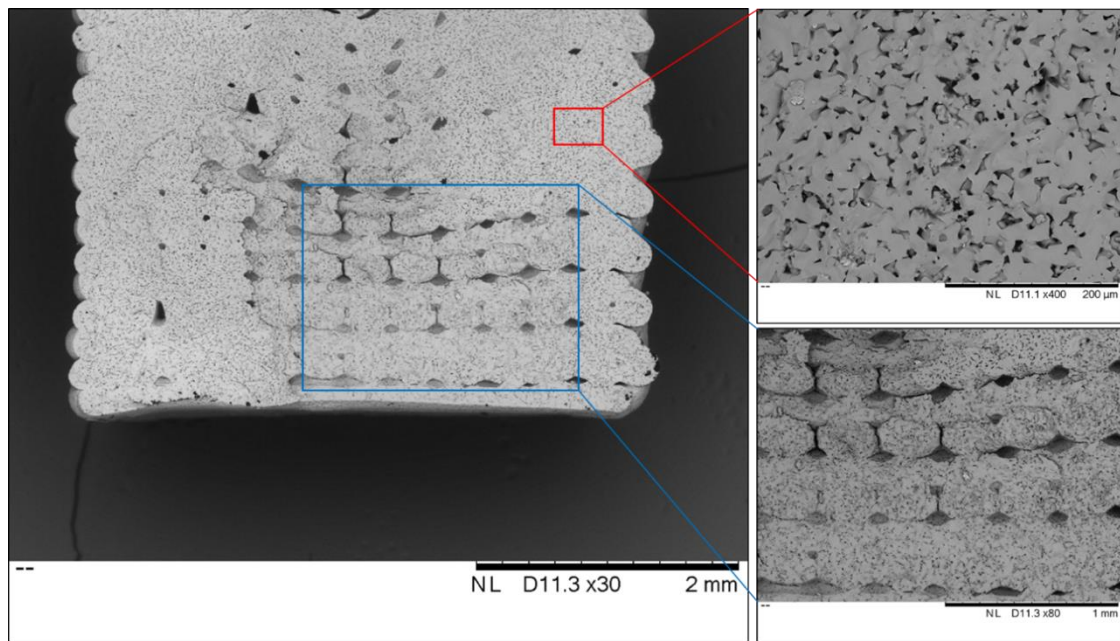


Figure 13: SEM images of the internal structure of a sintered B_4C beam fabricated from a paste formulation without C sintering aid, showing regularly spaced macro-pores between struts and a very high level of residual micro-porosity.

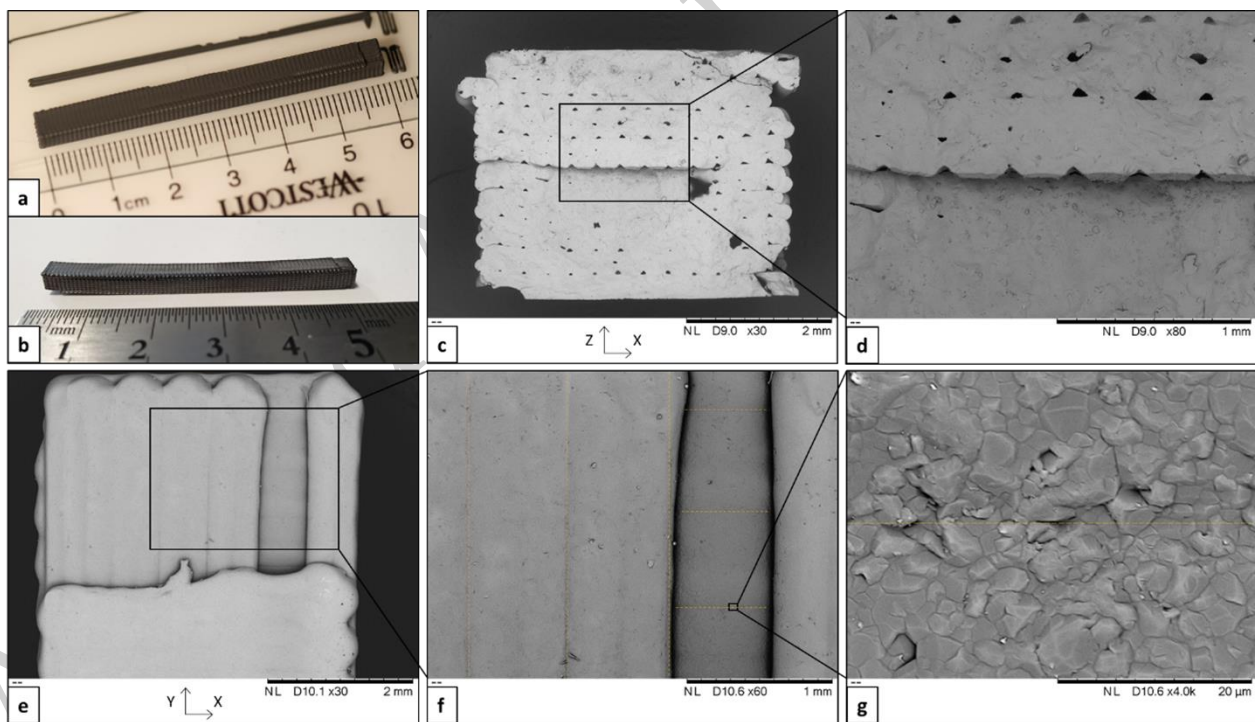


Figure 14: B_4C beam before (a) and after (b) sintering manufactured using a $406\ \mu\text{m}$ nozzle from a paste formulation containing 8 wt% carbon black relative to B_4C . Internal porosity occurred in the form of a three dimensional array of $100 - 200\ \mu\text{m}$ -wide inter-strut pores (c), although the rest of the structure appeared to be fully-dense (d). Top view of the beam showing three layers printed in a $0/90^\circ$ orientation (e); although printing lines were visible at the macro-scale (f) there was no obvious interface between grains at the micro-scale (g).

3.6. Surface roughness

The surface roughness of sintered specimens that were made using 584 μm and 406 μm extrusion nozzles was first observed using an SEM. **Figure 15** shows that clear printing lines were visible at the surface. Struts deposited using the 584 μm nozzle were approximately 550 μm wide while printing lines from the 406 μm orifice were ~ 330 μm wide.

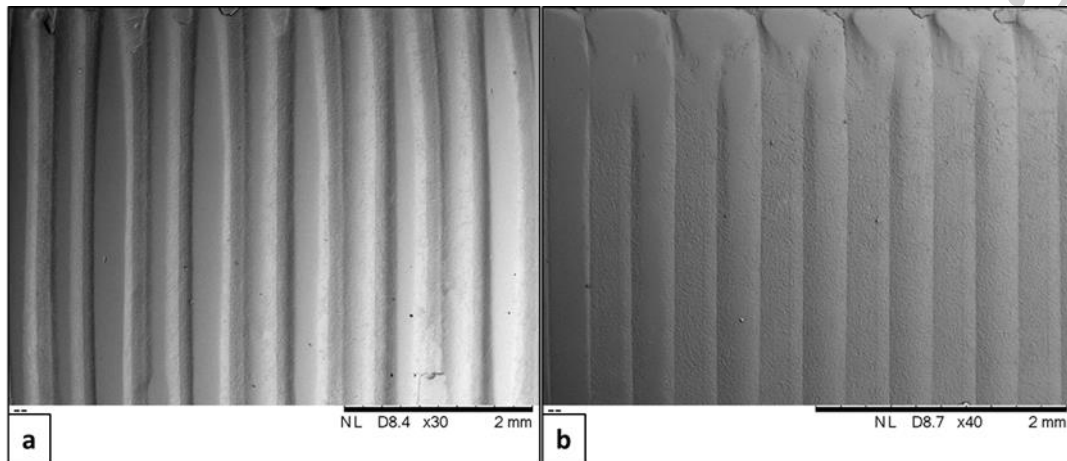


Figure 15: Top surface of multi-layer monolithic B_4C samples printed using the 584 μm (a) and 406 μm (b) extrusion nozzles.

Surface roughness was measured by line-scan profilometry after furnace sintering and examples of surface profile line-scans of 10-layer specimens are provided in **Figure 16**. Measurements were taken perpendicularly to individual printing lines, on the top, side and bottom surfaces of a sample produced using the 406 μm tip, and at the top surface of a sample made with the 584 μm orifice. The roughness of the side surface of the latter sample could not be recorded as the high slumping occurring upon paste deposition during DIW fabrication resulted in a distorted surface. Moreover, as discussed earlier, the bottom surface of all samples made with the 584 μm orifice were characterised by macro-pores that in some instances covered almost the entire bottom surface (**Figure 8**), making any surface roughness measurement meaningless. A summary table of the values of R_a and RMS roughness parameters that were obtained is provided in **Supporting Information**. The surface roughness of the top surface was significantly lower when reducing the diameter of the extrusion nozzle, with a R_a of 13.9 ± 0.7 μm for the 584 μm nozzle while it was reduced by 75% to 3.5 ± 0.2 μm when using the 406 μm orifice diameter. The surface roughness of the vertical side surface was twice as high as that of the horizontal top surface, with

a R_a of $7.4 \pm 1.2 \mu\text{m}$, while the bottom surface was much smoother, with a R_a of only $0.9 \pm 0.3 \mu\text{m}$, matching the roughness of the smooth glass slides that served as DIW substrate.

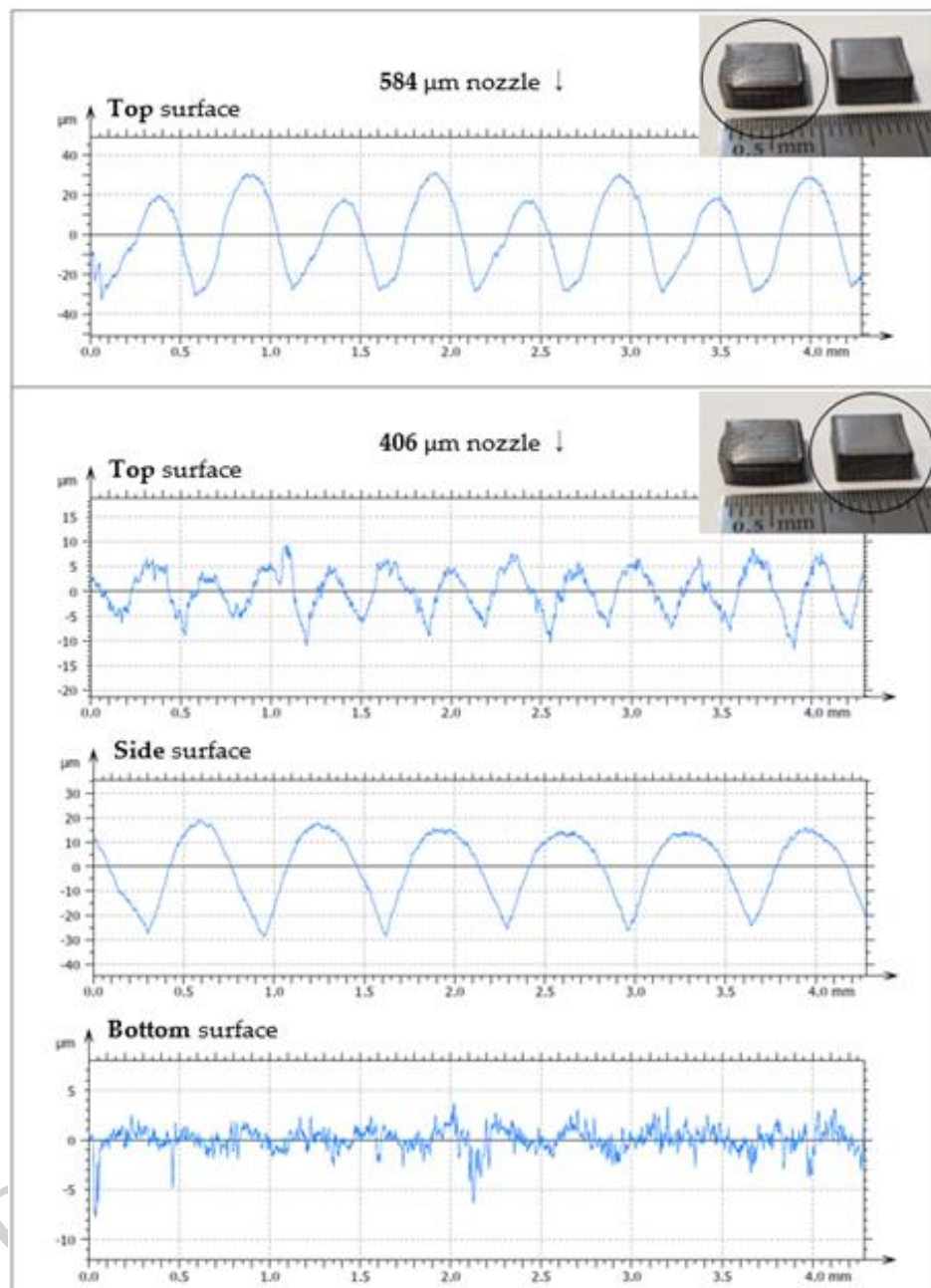


Figure 16: Surface profile of the top surface of a B_4C sample produced with the 584 μm nozzle, and of the top, side and bottom surfaces of a specimen made using the 406 μm orifice.

3.7. XRD

Figure 17 shows XRD scans of B_4C samples in both the green and sintered states, which provided a useful confirmation of the phases present at each stage of the manufacturing process. The characteristic peaks of the B_4C and the carbon phases (8 wt% carbon black additive relative to B_4C) are clearly identified on each graph. Furthermore, a peak at 19.2° on the XRD of the green sample, which could not be recognised by the analysis software, was identified as Pluronic F-127 by doing a separate XRD scan of raw Pluronic powder (**SI-3**). XRD of the sintered B_4C specimen confirmed the complete removal of Pluronic after heat treatments. The presence of free carbon in sintered boron carbide specimens suggests that the carbon black concentration of 8 wt% relative to B_4C was likely slightly too high, as not all the carbon reacted with the B_2O_3 present as a surface coating on B_4C particles. This was confirmed by the XRD scan of a C-free sintered specimen that did not display the characteristic peaks of carbon (**SI-4**). While on the one hand an excess of carbon may be detrimental to the mechanical properties of sintered B_4C , it does on the other hand promote diffusion during pressureless sintering by lowering significantly the melting point of B_4C at the grain boundaries and it also inhibits grain growth [56][2].

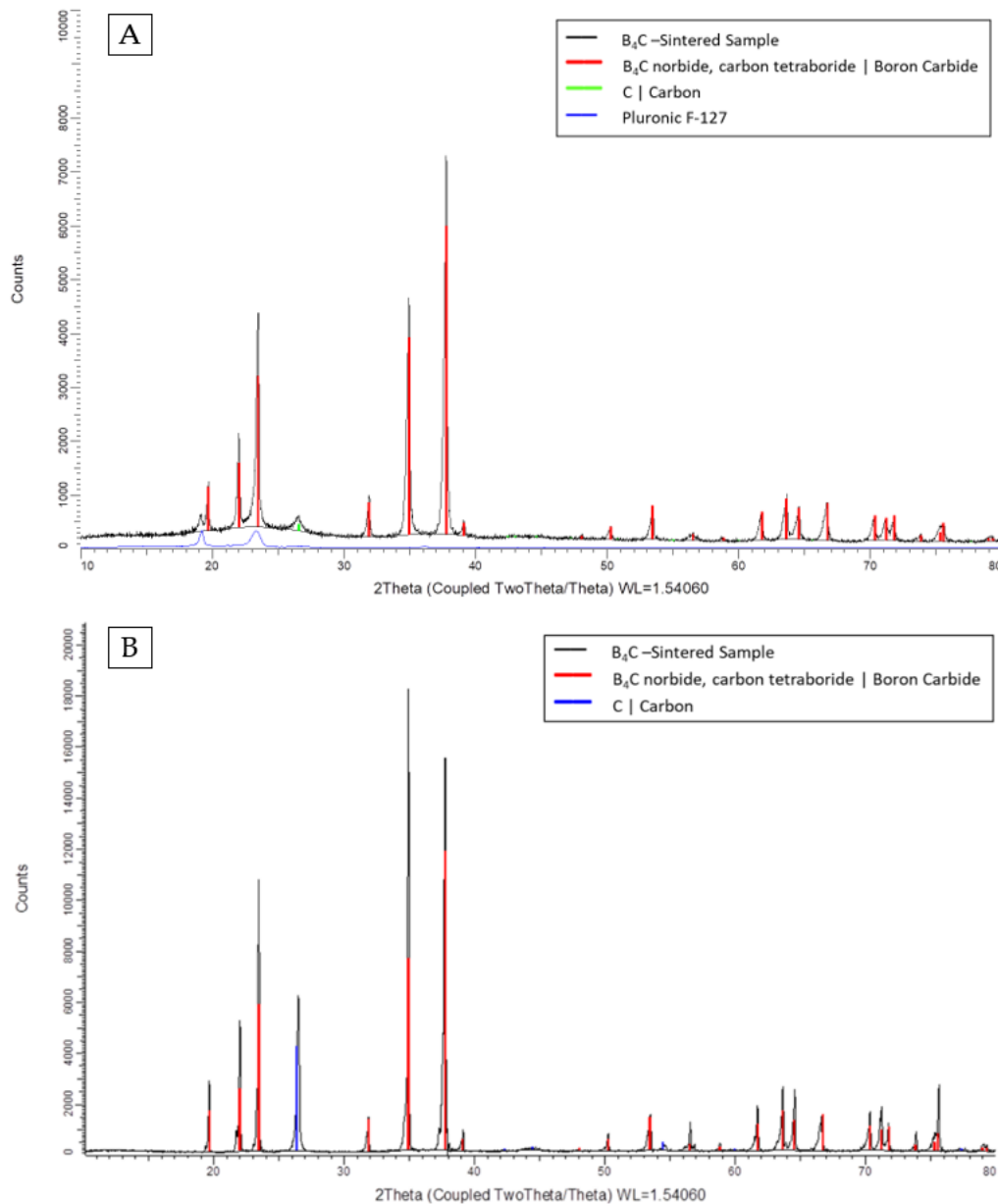


Figure 17: XRD scan of a B_4C sample in the green state with that of Pluronic F-127 underneath (A) and XRD of the same B_4C specimen after furnace sintering (B).

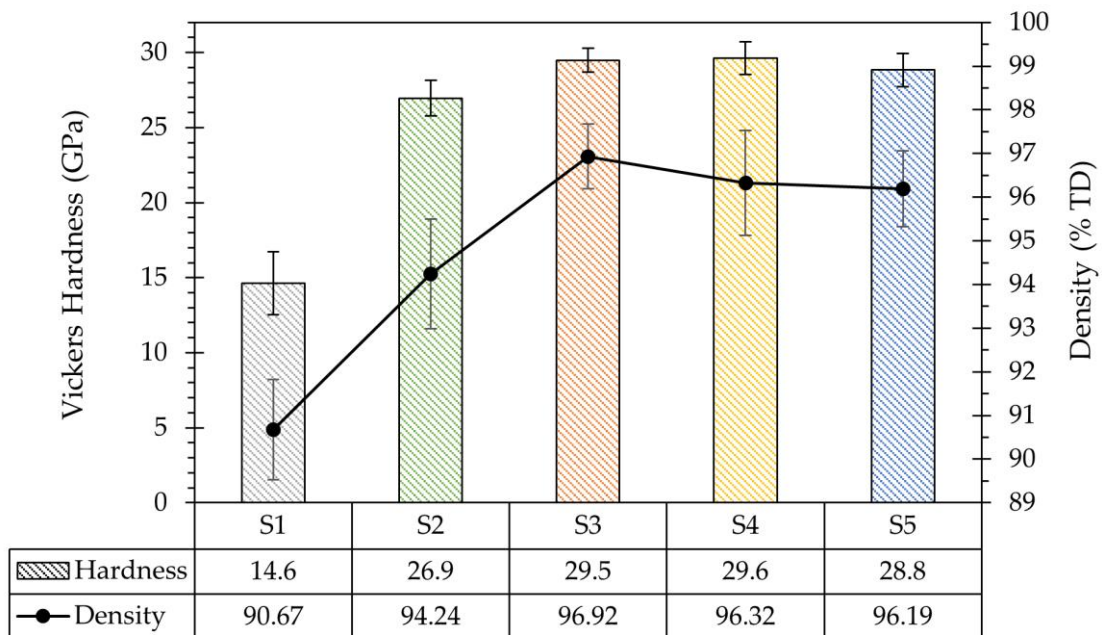
3.8. Vickers hardness

Vickers hardness measurements were carried out on the top surface of ground and polished monolithic 4-layer-thick samples fabricated using various paste formulations and printing parameters as detailed in **Table 4**. Results are displayed in **Figure 18**.

Table 4: Materials and printing characteristics of hardness samples.

Sample name	Paste formulation	B ₄ C powder	Carbon black (wt%)	GNPs (wt%)	Extrusion orifice diameter (μm)
S1	P1	F1500	0	0	406
S2	P2	F1500	8	0	584
S3	P2	F1500	8	0	406
S4	P3	F1500 / F3000	8	0	406
S5	P4	F1500 / F3000	8	1.5	406

The lowest density and hardness values of 90.7 ± 1.1 %TD and 14.6 ± 2.1 GPa, respectively, were obtained for carbon-free specimens printed using a 406 μm extrusion orifice diameter. Significantly higher densities and hardness values were obtained when carbon additives were added to the formulation. Indeed, sample **S2** had an average density of 94.2 ± 1.2 %TD and a Vickers hardness of 26.9 ± 1.2 GPa. Sample **S3**, which was built using a 406 μm orifice whereas **S2** was manufactured using a 584 μm nozzle, had a density of 96.9 ± 0.7 %TD and an average hardness of 29.5 ± 0.8 GPa, representing a ~3% increase in density and a ~10% higher average hardness. Finally, the density and hardness of samples **S4** and **S5** were on par with that of **S3** – within the margins of error. Therefore, as far as density and hardness were concerned, the 7:3 wt/wt mix of B₄C powder grades F1500/F3000 did not provide additional benefits over using the F1500 powder alone, nor did the addition of 1.5 wt% C-750 graphene nano-platelets.

**Figure 18:** Density and Vickers hardness of B₄C specimens made by DIW.

4. DISCUSSION

A relatively wide range of paste formulations with various ceramic powder loadings and Pluronic concentrations could be successfully extruded and shaped. Since each formulation resulted in its own set of rheological properties, in particular viscosity, elastic modulus and yield stress, printing parameters needed to be continuously adapted to accommodate the rheology of each paste. The pastes and printing parameters development and optimised in this work can be used as a good starting point by researchers or manufacturers that want to use DIW to manufacture boron carbide parts. However, it is highly recommended to always carry out rheological measurements of their pastes first and consider the specific requirements of their own printing platforms.

In most cases, critical macro-pore formation and macro-cracking occurred at the bottom surface of samples counting more than 3-4 layers due to the lack of evaporation pathways for the solvent underneath the sample when printing onto fully dense substrates. Significant improvements were obtained by using the smaller nozzle (406 μm rather than 584 μm diameter) as well as by using pastes of higher solids content. A trade-off needed to be reached between paste stiffness, for shape retention and structural integrity upon deposition, and paste fluidity. Small monolithic shapes benefited from using stiffer pastes with a quick drying rate to enable multiple passes over a given point in a short time interval without slumping of the printed structure. On the other hand, longer-aspect-ratio monoliths such as beams were less impacted by low paste stiffness due to the longer time elapsed between successive passes of the nozzle at a given point, which allowed enough time for struts to dry and harden.

This work investigated the use of various printing substrates with different materials, roughness and densities to control the drying rate of printed structures and avoid differential drying between the centre and the surface of monoliths. Another possible route that could be investigated would be heating up the print during deposition either a bottom-up (substrate heating) or a top-down (blown air, heat lamp) approach. However, the highly porous printing substrate showed that excessively fast drying rates caused severe warping and cracking during deposition; high drying temperatures would likely result in the same outcome. Nevertheless, future studies could investigate the influence of temperature and humidity on drying rates and cracking both during DIW and during post-DIW drying.

A smaller extrusion orifice diameter of 203 μm was also tested to improve the resolution of the printing process and to increase the surface-to-volume ratio of extruded struts to obtain faster drying kinetics for improved build strength. However, none of the tested formulations could be successfully extruded without defects when using this small orifice, mostly due to rapid nozzle clogging. Although higher

applied syringe pressures may have enabled extruding the pastes through the smaller nozzle, this would not have solved the main issues related to excessively fast drying and warping of struts upon extrusion. Further feedstock optimisation is therefore required to enable high-resolution DIW of B₄C pastes. A simple first step would be to ensure that particle agglomerates are completely broken up by applying an appropriate slurry milling step before Pluronic addition [57]. It has been suggested that the use of biphasic mixtures instead of colloidal gels could facilitate the use of smaller nozzle orifices to print even finer micro features [58]. Instead of extruding in air, deposition can also be carried out into an oil bath, which has been shown to enable the generation of filaments with diameters under 100 µm [59][38].

Densities that were obtained compared well with the literature on boron carbide manufactured by DIW; a density of ~90% TD was obtained for specimens without sintering aid, which is similar to that obtained by Eqtesadi *et al.* [46]. Significantly higher sintered densities were obtained after adding carbon black sintering aids, bringing the densities up between 94 and 97% TD depending on paste formulation and diameter of the extrusion nozzle. These densities were similar to that obtained by Eqtesadi *et al.* after CIP and SPS at 2100°C. Higher densities could be obtained in the current study even without CIP due to the fact that optimised amounts of carbon sintering aid were used and that firing was performed at 2275°C, which are both highly favourable to B₄C densification. However, it should be noted that these densities were obtained only with few-layer samples. Samples that counted more than 4 layers were characterised either by significant macro- and micro-porosity when using non-optimised printing parameters (**Figure 9**), or, when using optimised materials and printing parameters, by a dense microstructure but with the formation of a regular 3D array of inter-strut pores (**Figure 14**). The sintered density of 10-layer monoliths printed using the 406 µm extrusion orifice from optimised paste formulations was ~87% TD, which was higher than that obtained by Costakis *et al.* (82% TD) [45], due to a very high green density of ~58% TD. As expected, the Vickers hardness of B₄C components increased as density increased and is comparable to that of pressureless B₄C specimens reported in the literature [60][8], although it remained lower than HV values reported for uniaxial pressure-assisted spark plasma sintered B₄C [3][61].

Furthermore, the 1.5 wt% GNPs addition had seemingly no effect on neither density nor hardness, which could be due to the fact that GNPs may dissolve in B₄C at high sintering temperatures to form a solid solution, essentially reducing the function of GNPs to that of sintering aids rather than structural additives. It is also arguably unclear whether XG Sciences' grade C GNPs truly are graphene nanoplatelets. Indeed, true GNPs were recently defined as being 10 graphene layers or less [62] but a recent article showed that most GNPs commercially available worldwide would be better defined as nano-graphite platelets [63]. We would expect the number of graphene layers in GNPs and their oxygen content to be

the most influential parameters during B₄C sintering. Indeed, just like the B₂O₃ layer on B₄C particles reacts with free carbon during sintering to form B₄C and CO gas, thus enabling sintering to start at ~1350°C [64], it can be expected that the oxygen in GNPs would react with free carbon to form CO and CO₂ gas, which could be parasitic to the initial sintering of B₄C. Therefore, further research and more in-depth material characterisation would be required to better understand the interactions of graphene platelets with B₄C during high temperature sintering.

Finally, the surface roughness of DIW specimens was also greatly improved by using a smaller extrusion orifice; not only using the smaller nozzle led to a 75% decrease of the surface roughness of top surfaces, it also led to significant improvements in shape retention and decreased slumping at the edges, as shown in **Figure 6** and **Figure 16**. An Ra of $3.5 \pm 0.2 \mu\text{m}$ and $7.4 \pm 1.2 \mu\text{m}$ for the top and side surface, respectively, was obtained using the 406 μm extrusion nozzle, compared to a top surface Ra of $13.5 \pm 0.7 \mu\text{m}$ with the 584 μm nozzle. This would be improved even further by using As a comparison, Ghazanfari *et al.* used the CODE extrusion process [65] to produce alumina components with a Ra of 5.2 μm and 16.9 μm for the top and side surface of specimens with approximately 320 μm layer thickness, respectively, while specimens with approximately 80 μm layer thickness had the top and side surface Ra of 1.9 μm and 2.5 μm , respectively. Surface roughness values were also comparable to that of zirconia components produced using a commercial 3D printer based on inkjetting [66], which have a roughness of $12.5 > R_a > 1.6$ [67], but remain significantly higher than that of ceramics manufactured from lithography-based AM. For instance, Al₂O₃ specimens manufactured using a commercial DLP technology had a roughness comparable to that of injection moulded parts, yielding a Ra of 1.08 μm perpendicular to individual printing layers and only 0.36 μm in the plane of an individual layer [68].

5. CONCLUSIONS

Direct ink writing, an extrusion-based additive manufacturing technique, was investigated to produce near-net shaped monolithic boron carbide specimens by pressureless sintering. The effects of B₄C solids loading and Pluronic F-127 binder concentration on the rheological properties and printing behaviour of aqueous pastes as well as on the final quality and properties of printed specimens were studied. An increase in ceramic powder loading and/or binder concentration led to an increase in the yield stress, viscosity, storage modulus, and overall shape retention. Reducing the size of the extrusion nozzle from 584 μm to 406 μm led to significantly better shape retention, lower surface roughness, as well as higher density and hardness. A 203 μm printing orifice was also trialled but was unsuccessful due to faster drying

kinetics that occurred with smaller ceramic struts resulting in rapid warping and nozzle clogging. Carbon-black acted as an effective sintering aid to increase both density and hardness, while a 1.5 wt% addition of graphene nanoplatelets had no effect. The porosity of the printing substrate had a great influence over the drying rate and warpage of printing specimens. Several paste formulations were found to be suitable to produce B₄C monoliths by DIW, although printing issues and defects, such as nozzle clogging, cracks and pores were difficult to mitigate. Nevertheless, the [48 vol% B₄C / 17 wt% Pluronic] paste formulation, shaped using a 406 μm extrusion orifice, resulted in high sintered densities and hardness values. SEM imaging and μCT scanning were used for the first time to provide insight into the internal meso- and microstructure of B₄C components produced by DIW, showing that despite a defect-free external appearance and a fully dense internal microstructure, the formation of interstut porosity was difficult to prevent since a certain level of strut stiffness was required to prevent slumping and maintain high shape retention, whereas slumping is beneficial to strut merging.

There are many avenues for future studies to build up on this work to further improve DIW of B₄C, such as further optimising B₄C pastes to increase strut merging without sacrificing shape retention; formulating a B₄C paste that can be shaped using smaller extrusion nozzles (for instance 206 μm) to increase manufacturing resolution and decrease the size of printing defects; studying the fabrication of larger B₄C monoliths; investigating the effects on density and cracking of temperature and humidity during deposition and drying; and expanding mechanical testing to include flexural strength, compressive strength and Weibull analysis.

DECLARATIONS OF INTEREST

None.

ACKNOWLEDGEMENTS

This work was funded through the Engineering and Physical Sciences Research Council (EPSRC, UK) Centre for Doctoral Training in Additive Manufacturing and 3D Printing grant [EP/L01534X/1], sponsored by **AWE plc**, and performed under the auspices of the U.S. Department of Energy by **Lawrence Livermore National Laboratory** under Contract DE-AC52-07NA27344. The authors would like to thank Swetha Chandrasekaran at LLNL for providing the 3D printing files, Hannah Constantin at the University of Nottingham for performing the XRD, Robert Sampson and Naomi Stubbs at AWE for the sintering and μ CT scanning of B₄C specimens, respectively.

REFERENCES

- [1] V. Domnich, S. Reynaud, R. A. Haber, and M. Chhowalla, "Boron carbide: Structure, properties, and stability under stress," *J. Am. Ceram. Soc.*, vol. 94, no. 11, pp. 3605–3628, 2011.
- [2] A. K. Suri, C. Subramanian, J. K. Sonber, and T. S. R. C. Murthy, "Synthesis and consolidation of boron carbide: a review," *Int. Mater. Rev.*, vol. 55, no. 1, pp. 4–40, Jan. 2010.
- [3] W. Ji et al., "Sintering boron carbide ceramics without grain growth by plastic deformation as the dominant densification mechanism," *Sci. Rep.*, vol. 5, no. October, pp. 1–8, 2015.
- [4] X. Du et al., "Hot-pressing kinetics and densification mechanisms of boron carbide," *J. Am. Ceram. Soc.*, vol. 98, no. 5, pp. 1400–1406, 2015.
- [5] J. Pomerantz and T. Sano, "Characterization of Pressureless Sintered Boron Carbide." Army Research Laboratory, 2013.
- [6] S. Leo, C. Tallon, and G. V. Franks, "Aqueous and nonaqueous colloidal processing of difficult-to-densify ceramics: Suspension rheology and particle packing," *J. Am. Ceram. Soc.*, vol. 97, no. 12, pp. 3807–3817, 2014.
- [7] X. Li, D. Jiang, J. Zhang, Q. Lin, Z. Chen, and Z. Huang, "Pressureless sintering of boron carbide with Cr₃C₂ as sintering additive," *J. Eur. Ceram. Soc.*, vol. 34, no. 5, pp. 1073–1081, 2014.
- [8] M. Mashhadi, E. Taheri-Nassaj, and V. M. Sglavo, "Pressureless sintering of boron carbide," *Ceram. Int.*, vol. 36, no. 1, pp. 151–159, 2010.
- [9] T. K. Roy, C. Subramanian, and A. K. Suri, "Pressureless sintering of boron carbide," *Ceram. Int.*, vol. 32, no. 3, pp. 227–233, 2006.
- [10] B. R. Klotz, K. C. Cho, and R. J. Dowding, "Sintering Aids in the Consolidation of Boron Carbide (B₄C) by the Plasma Pressure Compaction (P2C) Method," *Mater. Manuf. Process.*, vol. 19, no. 4, pp. 631–639, Oct. 2004.
- [11] X. Shi, J. Cao, Z. Li, and D. Yan, "Effect of the Addition of Carbon on the Sintering Properties of Boron Carbide Ceramics prepared by Pressureless Sintering," in *3rd International Conference on Material, Mechanical and Manufacturing Engineering (IC3ME 2015)*, 2015, pp. 392–398.
- [12] I. Ceserano, Joseph and P. D. Calvert, "Freeforming objects with low-binder slurry," US006027326A, 2000.
- [13] T. a Baer, J. Cesarano III, P. Calvert, J. Cesarano, T. a Baer, and P. Calvert, "Recent Developments in Freeform Fabrication of Dense Ceramics From Slurry Deposition," in *Proceedings of Solid Freeform Fabrication Symposium*, 1997, pp. 25–32.

- [14] B. A. Tuttle et al., "Robocast Pb(Zr_{0.95}Ti_{0.05})O₃ Ceramic Monoliths and Composites," *J. Am. Ceram. Soc.*, vol. 74, pp. 872–874, 2001.
- [15] J. E. Smay, J. Cesarano, and J. A. Lewis, "Colloidal inks for directed assembly of 3-D periodic structures," *Langmuir*, vol. 18, no. 14, pp. 5429–5437, 2002.
- [16] Q. Fu, E. Saiz, and A. P. Tomsia, "Direct Ink Writing of Highly Porous and Strong Glass Scaffolds for Load-bearing Bone Defects Repair and Regeneration," *Acta Biomater.*, vol. 7, no. 10, pp. 3547–3554, 2011.
- [17] M. Acosta, V. L. Wiesner, C. J. Martinez, R. W. Trice, and J. P. Youngblood, "Effect of polyvinylpyrrolidone additions on the rheology of aqueous, highly loaded alumina suspensions," *J. Am. Ceram. Soc.*, vol. 96, no. 5, pp. 1372–1382, 2013.
- [18] S. S. Nadkarni and J. E. Smay, "Concentrated barium titanate colloidal gels prepared by bridging flocculation for use in solid freeform fabrication," *J. Am. Ceram. Soc.*, vol. 89, no. 1, pp. 96–103, 2006.
- [19] E. Feilden, E. G. T. Blanca, F. Giuliani, E. Saiz, and L. Vandeperre, "Robocasting of structural ceramic parts with hydrogel inks," *J. Eur. Ceram. Soc.*, vol. 36, no. 10, pp. 2525–2533, 2016.
- [20] F. J. Martínez-Vázquez, A. Pajares, and P. Miranda, "A simple graphite-based support material for robocasting of ceramic parts," *J. Eur. Ceram. Soc.*, vol. 38, no. 4, pp. 2247–2250, 2018.
- [21] J. Franco, P. Hunger, M. E. Launey, A. P. Tomsia, and E. Saiz, "Direct-Write Assembly of Calcium Phosphate Scaffolds Using a Water-Based Hydrogel," *Acta Biomater.*, vol. 6, no. 1, pp. 218–228, 2010.
- [22] P. Miranda, E. Saiz, K. Gryn, and A. P. Tomsia, "Sintering and robocasting of β -tricalcium phosphate scaffolds for orthopaedic applications," *Acta Biomater.*, vol. 2, no. 4, pp. 457–466, 2006.
- [23] C. Slots et al., "Simple additive manufacturing of an osteoconductive ceramic using suspension melt extrusion," *Dent. Mater.*, vol. 33, no. 2, pp. 198–208, 2017.
- [24] E. Saiz, L. Gremillard, G. Menendez, P. Miranda, K. Gryn, and A. P. Tomsia, "Preparation of porous hydroxyapatite scaffolds," *Mater. Sci. Eng. C*, vol. 27, no. 3, pp. 546–550, 2007.
- [25] M. Houmard, Q. Fu, M. Genet, E. Saiz, and A. P. Tomsia, "On the structural, mechanical, and biodegradation properties of HA/ β -TCP robocast scaffolds," *J. Biomed. Mater. Res. - Part B Appl. Biomater.*, vol. 101, no. 7, pp. 1233–1242, 2013.
- [26] Y. Xie et al., "Net shape fabrication of calcium phosphate scaffolds with multiple material domains," *Biofabrication*, vol. 8, p. 015005, 2016.
- [27] C. Petit et al., "Fracture behavior of robocast HA/ β -TCP scaffolds studied by X-ray tomography and finite element modeling," *J. Eur. Ceram. Soc.*, vol. 37, no. 4, pp. 1735–1745, 2017.

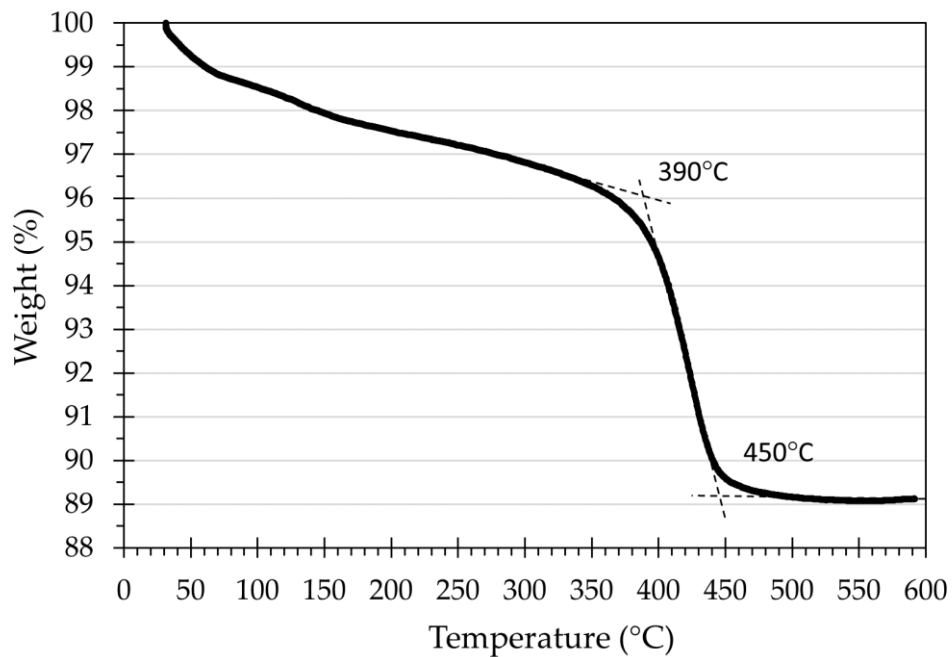
- [28] C. F. Marques et al., "Biphasic calcium phosphate scaffolds fabricated by direct write assembly: Mechanical, anti-microbial and osteoblastic properties," *J. Eur. Ceram. Soc.*, vol. 37, no. 1, pp. 359–368, 2017.
- [29] H. Shao et al., "3D robocasting magnesium-doped wollastonite/TCP bioceramic scaffolds with improved bone regeneration capacity in critical sized calvarial defects," *J. Mater. Chem. B*, vol. 5, no. 16, pp. 2941–2951, 2017.
- [30] Z. Fu et al., "Robocasting of carbon-alumina core-shell composites using co-extrusion," *Rapid Prototyp. J.*, vol. 23, no. 2, pp. 423–433, 2017.
- [31] X. Liu, M. N. Rahaman, G. E. Hilmas, and B. Sonny Bal, "Mechanical properties of bioactive glass (13-93) scaffolds fabricated by robotic deposition for structural bone repair," *Acta Biomater.*, vol. 9, no. 6, pp. 320–331, 2013.
- [32] S. M. Olhero, H. R. Fernandes, C. F. Marques, B. C. G. Silva, and J. M. F. Ferreira, "Additive manufacturing of 3D porous alkali-free bioactive glass scaffolds for healthcare applications," *J. Mater. Sci.*, vol. 52, no. 20, pp. 12079–12088, 2017.
- [33] S. Eqtesadi, A. Motealleh, R. Wendelbo, A. L. Ortiz, and P. Miranda, "Reinforcement with reduced graphene oxide of bioactive glass scaffolds fabricated by robocasting," *J. Eur. Ceram. Soc.*, vol. 37, no. 12, pp. 3695–3704, 2017.
- [34] P. Biswas, S. Mamatha, S. Naskar, Y. S. Rao, R. Johnson, and G. Padmanabham, "3D extrusion printing of magnesium aluminate spinel ceramic parts using thermally induced gelation of methyl cellulose," *J. Alloys Compd.*, vol. 770, pp. 419–423, 2019.
- [35] S. L. Morissette, J. a Lewis, J. Cesarano, D. B. Dimos, and T. Y. Baer, "Solid Freeform Fabrication of Aqueous Alumina-Poly(vinyl alcohol) Gelcasting Suspensions," *J. Am. Ceram. Soc.*, vol. 83, no. 10, pp. 2409–2416, 2000.
- [36] L. Rueschhoff, W. Costakis, M. Michie, J. Youngblood, and R. Trice, "Additive Manufacturing of Dense Ceramic Parts via Direct Ink Writing of Aqueous Alumina Suspensions," *Int. J. Appl. Ceram. Technol.*, vol. 13, no. 5, pp. 821–830, 2016.
- [37] T. Schlordt, F. Keppner, N. Travitzky, and P. Greil, "Robocasting of alumina lattice truss structures," *J. Ceram. Sci. Technol.*, vol. 3, no. 2, pp. 81–88, 2012.
- [38] T. Schlordt, S. Schwanke, F. Keppner, T. Fey, N. Travitzky, and P. Greil, "Robocasting of alumina hollow filament lattice structures," *J. Eur. Ceram. Soc.*, vol. 33, no. 15–16, pp. 3243–3248, 2013.
- [39] J. Azuaje et al., "An efficient and recyclable 3D printed α -Al₂O₃ catalyst for the multicomponent assembly of bioactive heterocycles," *Appl. Catal. A Gen.*, vol. 530, pp. 203–210, 2017.

- [40] J. Smay and J. Cesarano, "Directed Colloidal Assembly of Linear and Annular Lead Zirconate Titanate Arrays," *J. Am. ...*, vol. 95, pp. 290–308, 2008.
- [41] J. N. Stuecker, J. Cesarano, and D. A. Hirschfeld, "Control of the viscous behavior of highly concentrated mullite suspensions for robocasting," *J. Mater. Process. Technol.*, vol. 142, no. 2, pp. 318–325, 2003.
- [42] G. P. He, D. A. Hirschfeld, J. Cesarano III, and J. N. Stuecker, "Robocasting and Mechanical Testing of Aqueous Silicon Nitride Slurries," 2000.
- [43] S. Zhao, W. Xiao, M. N. Rahaman, D. O'Brien, J. W. Seitz-Sampson, and B. Sonny Bal, "Robocasting of silicon nitride with controllable shape and architecture for biomedical applications," *Int. J. Appl. Ceram. Technol.*, vol. 14, no. 2, pp. 117–127, 2017.
- [44] A. Kruisová et al., "Ultrasonic bandgaps in 3D-printed periodic ceramic microlattices," *Ultrasonics*, vol. 82, pp. 91–100, 2018.
- [45] W. J. Costakis, L. M. Rueschhoff, A. I. Diaz-Cano, J. P. Youngblood, and R. W. Trice, "Additive manufacturing of boron carbide via continuous filament direct ink writing of aqueous ceramic suspensions," *J. Eur. Ceram. Soc.*, vol. 36, no. 14, pp. 3249–3256, 2016.
- [46] S. Eqtesadi et al., "Fabricating geometrically-complex B₄C ceramic components by robocasting and pressureless spark plasma sintering," *Scr. Mater.*, vol. 145, pp. 14–18, 2018.
- [47] S. Chandrasekaran et al., "Additive manufacturing of graded B₄C-Al cermets with complex shapes," *Mater. Des.*, vol. 188, p. 108516, 2020.
- [48] Y. Lakhdar, C. Tuck, J. Binner, A. Terry, and R. Goodridge, "Additive manufacturing of advanced ceramic materials," *Prog. Mater. Sci.*, vol. 116, p. 100736, 2021.
- [49] R. Lu, S. Chandrasekaran, W. L. Du Frane, R. L. Landingham, M. A. Worsley, and J. D. Kuntz, "Complex shaped boron carbides from negative additive manufacturing," *Mater. Des.*, vol. 148, pp. 8–16, 2018.
- [50] XG Sciences Inc., "xGnP® Graphene Nanoplatelets – Grade C." 2018.
- [51] A. Diaz-Cano, R. W. Trice, and J. P. Youngblood, "Stabilization of highly-loaded boron carbide aqueous suspensions," *Ceram. Int.*, vol. 43, no. 12, pp. 8572–8578, 2017.
- [52] E. C. Society, F. Science, and L. Ls, "Experimental Studies of Particle Packing and Sintering Behaviour of Monosize and Bimodal Spherical Silica Powders," *J. Eur.*, vol. 11, pp. 1–7, 1993.
- [53] W. Du, M. Singh, and D. Singh, "Binder jetting additive manufacturing of silicon carbide ceramics : Development of bimodal powder feedstocks by modeling and experimental," *Ceram. Int.*, vol. 46, no. 12, pp. 19701–19707, 2020.

- [54] ASTM Standard B311-17, "Standard Test Method for Density of Powder Metallurgy (PM) Materials Containing Less Than Two Percent Porosity." ASTM International, West Conshohocken, PA, USA, 2017.
- [55] ASTM Standard C1327-15, "Standard Test Method for Vickers Indentation Hardness of Advanced Ceramics." ASTM International, West Conshohocken, PA, USA, 2015.
- [56] H. Suzuki, T. Hase, and T. Maruyama, "Effect of Carbon on Sintering of Boron Carbide," *Yogyo-Kyokai-Shi (J. Ceram. Soc. Jpn)*, vol. 87, no. 8, pp. 430–433, 1979.
- [57] Y. Lakhdar, C. Tuck, A. Terry, and R. Goodridge, "Dispersion and stability of colloidal boron carbide suspensions," *Ceram. Int.*, vol. 46, no. 18, pp. 27957–27966, 2020.
- [58] J. C. Conrad, S. R. Ferreira, J. Yoshikawa, R. F. Shepherd, B. Y. Ahn, and J. A. Lewis, "Designing colloidal suspensions for directed materials assembly," *Curr. Opin. Colloid Interface Sci.*, vol. 16, no. 1, pp. 71–79, 2011.
- [59] J. A. Lewis, "Direct ink writing of 3D functional materials," *Adv. Funct. Mater.*, vol. 16, no. 17, pp. 2193–2204, 2006.
- [60] A. Nikravan, H. R. Baharvandi, F. B. Jebelli, H. Abdizadeh, and N. Ehsani, "Microstructure and mechanical properties of pressureless sintered B 4C-C composite using phenolic resin," *Proc. SPIE - Int. Soc. Opt. Eng.*, vol. 6423, pp. 1–7, 2007.
- [61] X. Li, D. Jiang, J. Zhang, Q. Lin, Z. Chen, and Z. Huang, "Densification behavior and related phenomena of spark plasma sintered boron carbide," *Ceram. Int.*, vol. 40, no. 3, pp. 4359–4366, 2014.
- [62] A. J. Pollard et al., "Characterisation of the Structure of Graphene - Good Practice Guide N. 145," 2017.
- [63] A. P. Kauling et al., "The Worldwide Graphene Flake Production," *Adv. Mater.*, vol. 30, no. 1803784, pp. 1–6, 2018.
- [64] W. Li, A. Ghazanfari, D. McMillen, M. C. Leu, G. E. Hilmas, and J. Watts, "Characterization of zirconia specimens fabricated by ceramic on-demand extrusion," *Ceram. Int.*, vol. 44, no. 11, pp. 12245–12252, 2018.
- [65] H. Lee and R.F. Speyer, "Pressureless Sintering of Boron Carbide," *J. Am. Ceram. Soc.*, vol. 86, no. 9, pp. 1468–1473, 2003.
- [66] XJet, "XJet systems," 2017. [Online]. Available: <http://xjet3d.com/systems/>. [Accessed: 23-Nov-2017].
- [67] XJet, "XJet 500Ceramic Specifications," Rehovot, Israel, 2017.
- [68] M. Schwentenwein and J. Homa, "Additive manufacturing of dense alumina ceramics," *Int. J. Appl.*

Accepted Author Manuscript

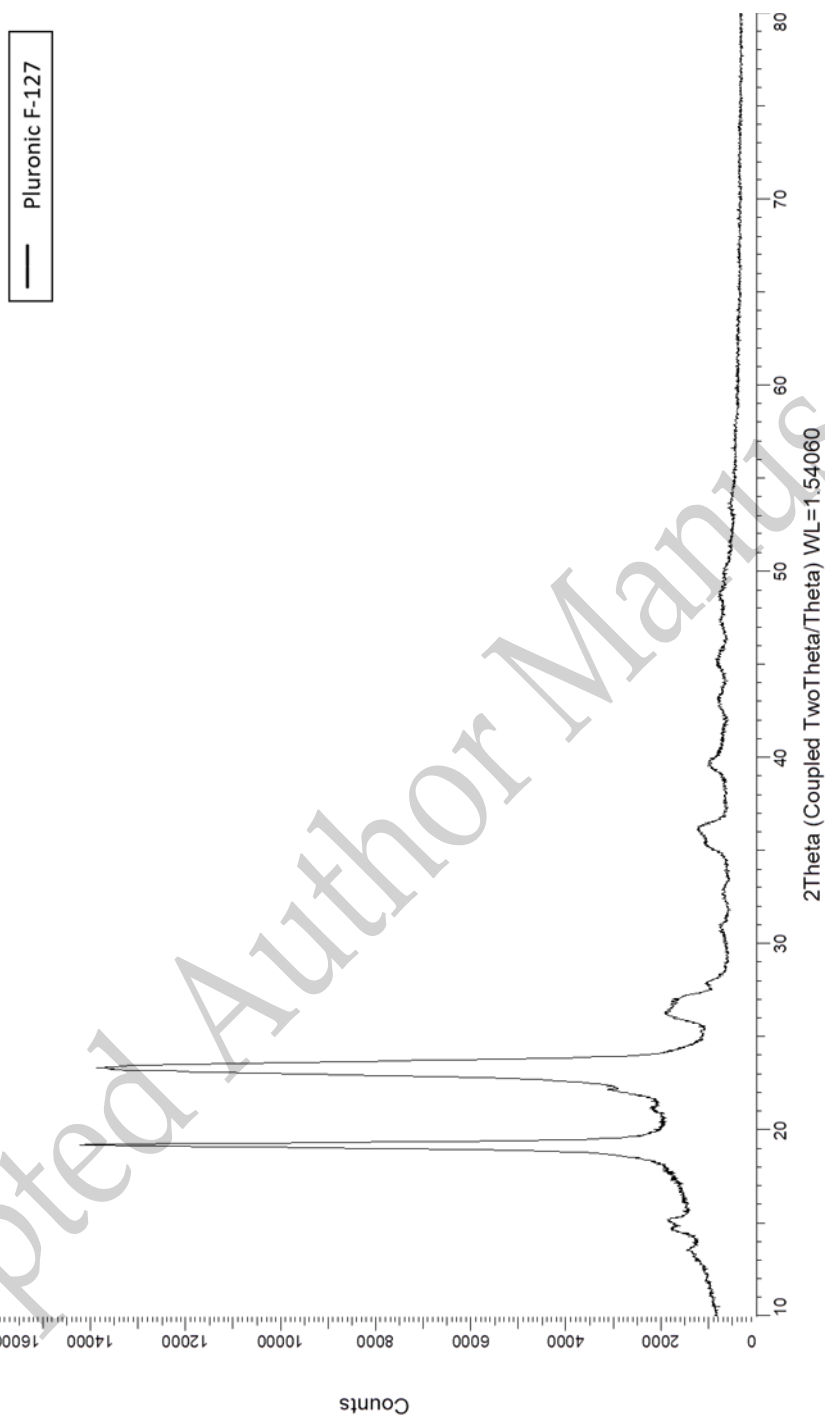
SUPPORTING INFORMATION



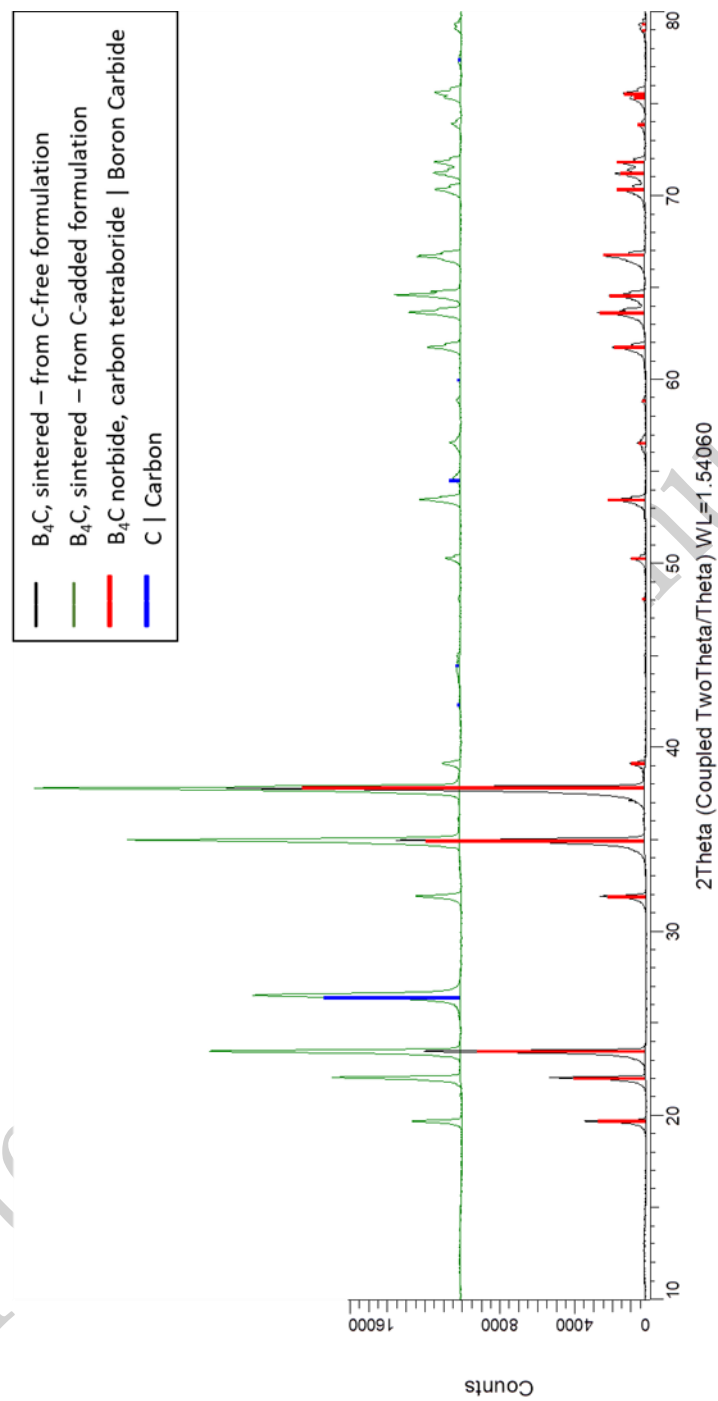
SI-1: TGA of a DIW green B₄C sample. Organics (PEI and Pluronic) were completely removed from green parts at 500°C.

SI-2: Summary of the surface roughness parameters, *Ra* and *RMS*, of the top, side and bottom surfaces of sintered specimens produced using the 584 and 406 μm diameter orifices.

Nozzle diameter	584 μm		406 μm					
	Top		Top		Side		Bottom	
Roughness parameter	<i>Ra</i>	<i>RMS</i>	<i>Ra</i>	<i>RMS</i>	<i>Ra</i>	<i>RMS</i>	<i>Ra</i>	<i>RMS</i>
Sample 1	13.7	15.4	3.4	3.9	9.0	10.8	0.59	0.77
Sample 2	14.9	16.8	3.5	4.0	7.5	8.8	0.95	1.30
Sample 3	13.8	15.5	3.3	3.9	6.0	7.3	0.83	1.07
Sample 4	13.2	14.6	3.7	4.2	7.3	8.5	1.41	1.98
AVG.	13.9	15.6	3.5	4.0	7.4	8.9	0.94	1.28
Std. dev.	0.7	0.9	0.2	0.1	1.2	1.5	0.3	0.5



SI-3: XRD scan of Pluronic F-127.



SI-4: XRD scan of a B₄C specimens made using pastes containing 8 wt%_{B₄C} of carbon black sintering aid (top) and a carbon additive-free paste (bottom).